



**Babeş-Bolyai University, Cluj-Napoca, Romania**

**Doctoral School of Chemical Engineering**

*In collaboration with*

**Technical University of Dortmund (TU Dortmund University), Dortmund,  
Germany**

**Leibniz Institute for Catalysis e.V. (LIKAT), Rostock, Germany**

*within the European Doctorate Internship*

**Summary of the Ph.D. Thesis**

**Design of Titanium-based Catalysts for Photocatalytic  
Applications. Flow and Kinetic Studies in a Multichannel  
Falling Film Micro-Photoreactor**

Author: Ing. Biborka Boga

PhD Supervisor:

Prof. Dr-Ing. Vasile-Mircea Cristea

PhD Supervisors within the European Doctorate Internship:

Prof. Dr.-Ing. Norbert Kockmann (TU Dortmund University)

Prof. Dr. Jennifer Strunk (LIKAT and Technical University of Munich)

**2024**

## Content of the "Summary of the Ph.D. Thesis"

	3
<b>Chapter 1 – Introduction. Motivation and Research Objectives.</b>	
<b>Chapter 2 – Scientific contributions</b>	
(2.1) Experimental data-driven and phenomenological modeling approaches targeting the enhancement of CaTiO <sub>3</sub> photocatalytic efficiency	9
(2.2) Role of SrCO <sub>3</sub> on photocatalytic performance of SrTiO <sub>3</sub> -SrCO <sub>3</sub> composites	16
(2.3) Design of SrTiO <sub>3</sub> -based catalysts for photocatalytic CO <sub>2</sub> reduction	22
(2.4) Experimental and numerical investigations of flow behavior in an open falling film microreactor equipped with curved flow splitting elements	30
(2.5) Photocatalytic antibiotic degradation in coated open microchannels by applying 2D and 3D flow modeling with kinetics	39
<b>Chapter 3 – Final conclusions</b>	40
<b>Chapter 4 – Bibliography</b>	45

**Keywords:** photocatalytic CO<sub>2</sub> reduction, solar fuels, neural network models, SrTiO<sub>3</sub>-based catalyst, structure-function correlation, CaTiO<sub>3</sub>, microchannel, multiphase flow, backflow, TiO<sub>2</sub>-coated microchannels, ciprofloxacin, numerical, coupled mass and momentum conservation law, CFD, optiSLang.

## Content of the Ph.D. Thesis

<b>Acknowledgment</b>	1
<b>Summary</b>	3
<b>Rezumat</b>	7
<b>Chapter 1 – Introduction</b>	
(1.1) Motivation	9
(1.2) Photochemical reaction systems – Excitonic chemical conversion system	9
(1.2.1) Principle of light-driven heterogeneous catalytic reactions	10
(1.2.2) Approaches targeting the design of photocatalysts	12
(1.2.3) Titanium-based catalysts	13
(1.3) Photocatalytic reactors for wastewater treatment	16
(1.3.1) Classification of photoreactors for wastewater treatment	16
(1.3.2) Photocatalytic microreactors with applications in wastewater treatment	18
(1.4) Selected aspects of the mathematical modeling of photocatalytic reactors	19
(1.5) General and specific research objectives	21
<b>Chapter 2 – Scientific contributions</b>	
(2.1) Experimental data-driven and phenomenological modeling approaches targeting the enhancement of CaTiO <sub>3</sub> photocatalytic efficiency	24
(2.2) Role of SrCO <sub>3</sub> on photocatalytic performance of SrTiO <sub>3</sub> -SrCO <sub>3</sub> composites	57
(2.3) Design of SrTiO <sub>3</sub> -based catalysts for photocatalytic CO <sub>2</sub> reduction	81
(2.4) Experimental and numerical investigations of flow behavior in an open falling film microreactor equipped with curved flow splitting elements	144
(2.5) Photocatalytic antibiotic degradation in coated open microchannels by applying 2D and 3D flow modeling with kinetics	185
<b>Chapter 3 – Concluding Remark and Personal Contributions</b>	221
<b>Chapter 4 – Publication List, Dissemination of the Results</b>	
(4.1) Publication list	226
(4.2) Conferences, colloquiums	228
<b>Bibliography</b>	229

## **Chapter 1. Introduction**

### **Motivation**

"Let there be light!"

Light has an essential role in evolution of present form of life on Earth [1]. Among the light-assisted processes, photosynthesis has a considerable importance [2]. Natural photosynthesis is considered as an inspiration source for the development of solar, photocatalytic and photoelectrochemical cells, and photo-rechargeable battery technologies, respectively [2]. In the first part of this work, the focus is on the conversion of light into chemical energy. In phototrophic organisms, solar-to-chemical energy conversion takes place only in highly organized and complex systems, also called as photosynthetic reaction center proteins [3]. Mimicking the Nature, photocatalysts (i.e., semiconductor metal oxides) with appropriate electronic structure were designed and applied, which is known as artificial photosynthesis or photocatalytic CO<sub>2</sub> reduction. Artificial photosynthesis can be considered as a promising and environmentally friendly solution for overcoming two major environmental problems, namely increasing atmospheric CO<sub>2</sub> concentration (i.e., 425 ppm [4]), and increasing energy demand [5], since it is based on the conversion of atmospheric CO<sub>2</sub> into valuable fuels (CH<sub>4</sub> or higher hydrocarbons).

Furthermore, beyond the increasing atmospheric CO<sub>2</sub> concentration and energy demand, the quality of drinking water is another concerning aspect which requires urgent actions. The occurrence of contaminants of emerging concern (CECs) – endocrine disruptors, pharmaceuticals – in drinking water was proven by recent studies [6]. For example, the relatively low removal efficiency of active pharmaceutical ingredients and its consequences, i.e., development of antimicrobial resistance [7] may lead to considerable health issues. Among the well-known techniques aiming the removal of CECs from wastewaters (i.e., adsorption, ion-exchange, membrane technology), advanced oxidation processes (AOPs), and more precisely heterogeneous photocatalysis received considerable attention in water [8] and air purification [9].

Although both processes – photocatalytic CO<sub>2</sub> reduction and photodegradation of CECs – are based on the application of a (photo)catalyst and the usage of solar energy, however the differences in thermodynamic and kinetic aspects must be discussed.

### **Principle of light-driven heterogeneous catalytic reactions**

The heterogeneous photocatalytic technologies are classified into two main categories, namely purification technologies and synthetic pathways [10]. While water treatment and air purification belong to the category of purification technologies, energy generation, organic synthesis and alternative fuels take part of the group of synthetic pathways [10]. Two photocatalytic applications, gas-phase photoreduction of CO<sub>2</sub> and photooxidation of organic contaminants (in aqueous solution), will be covered in this thesis. The principle of heterogeneous photocatalytic reactions will be discussed prior to the presentation of the distinctive features of the latter two processes.

Heterogeneous photocatalysis is a complex process, which takes place in the presence of photocatalysts under electromagnetic irradiation. The schematic representation of the elementary steps within the heterogeneous photocatalysis using a semiconductor photocatalyst is given in Figure 1. The first step is based on the light-induced excitation of the photocatalyst with the condition that the energy of irradiation (i.e.,  $E_{\text{photon}} = h\nu$ ) is higher or equivalent with the band gap energy ( $\Delta E_g$ ) of the photocatalyst (Step 1). This latter leads to the translocation of the photoexcited  $e^-$  from the valance band (VB) to the conduction band (CB) of semiconductor photocatalyst, which results in charge separation (i.e.,  $e^-$  in the CB and  $h^+$  in the VB, Step 2). The photogenerated charge carriers (i.e.,  $e^-$ ,  $h^+$ ) migrate to the surface of the catalyst (Step 3), followed by their participation in further redox reactions with the species adsorbed on the surface of the catalyst (Step 4) [11, 12]. The redox reactions with the photogenerated charge carriers (i.e.,  $e^-_{\text{CB}}$ ,  $h^+_{\text{VB}}$ ) are constrained to the following condition: "the CB of the photocatalyst must be more negative than the reduction potential" (of the reduction potential) and "the VB must be more positive than the oxidation potential" (of the targeted oxidation reaction) [11]. Finally, the products are desorbed (Step 5) [12].

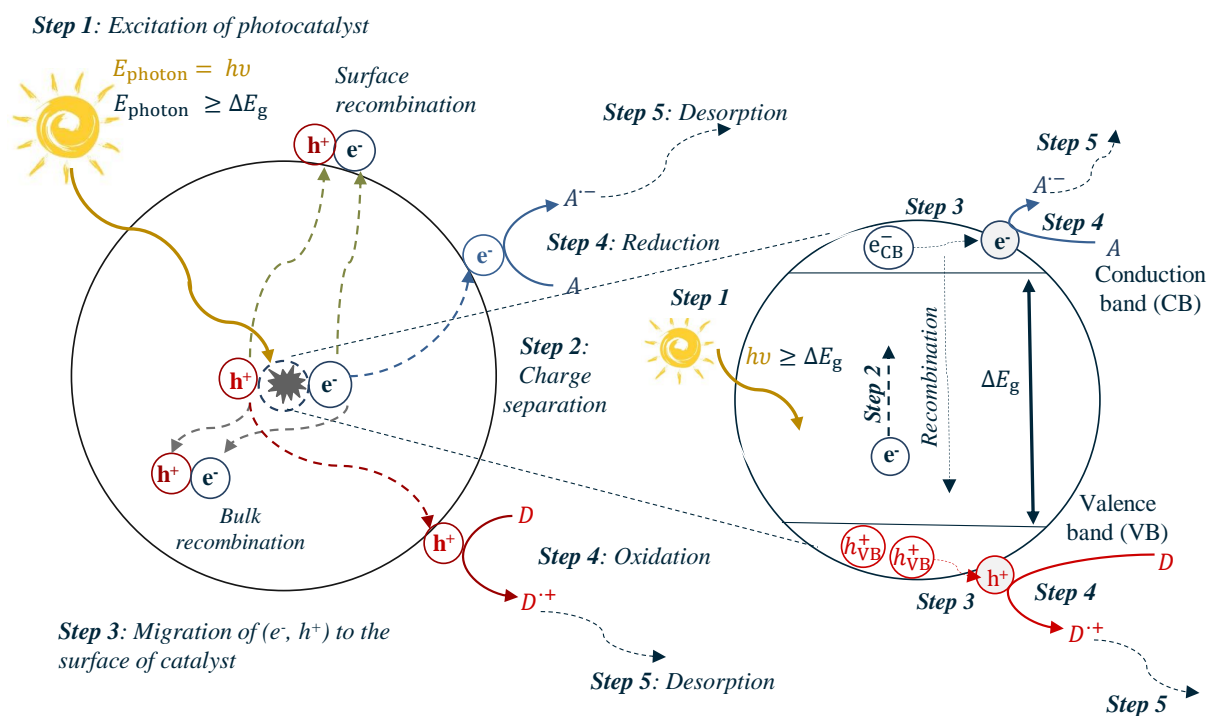


**Figure 1.** Schematic representation of photoexcitation, possible recombination pathways of the photogenerated charge carriers, and redox reactions in a solid semiconductor photocatalyst (left figure); elementary steps of heterogeneous photocatalysis considering the band structure of a semiconductor photocatalyst (right figure) (Inspired from [10, 11, 13])\*

\* Significance of notation in Figure 1: A – acceptor, D – donor

## **Photocatalytic reactors for wastewater treatment**

In addition to the development of catalysts and reaction engineering aspects, the design of photoreactors is considered as one of the pillars of the heterogeneous photocatalysis [14]. Herein, the focus will be on the photocatalytic reactors for wastewater treatment applications. The importance of the development and improvement in case of photocatalytic reactors (for wastewater treatment) is given by the following reasons: (1) "innovative reactor designs" may "improve the activity of the photocatalyst" [15], (2) it may open new perspectives towards transposing the technology from "research and development" stage to real-world implementation [15]. However, the potential for improvement of the photocatalytic process *via* reactor design has been largely overlooked [15].

The PhD thesis provides an overview of selected classification of the photoreactors in association with their advantages and disadvantages. The effectiveness of the photocatalytic process is influenced by several parameters, namely flow rate (in case of continuous operation) [16], initial concentration of the contaminant in the aqueous solution [17], photocatalyst loading [18], pH of the reaction mixture [18], characteristics of the irradiations source – power and wavelength [15], fluid dynamics regime [15], etc.

Moreover, the scaling-up of these photoreactors from the lab or pilot scale to the industrial scale still poses challenges to the scientific community [19]. Their "full-scale application" was constrained not only by the reactor design, or the issues related to the catalyst, but also to "engineering factors", such as "fluid pumping energy, pressure drop, temperature, tubing materials, and interfering effect of water and matrix species" [15]. Regardless to the bottlenecks, several outstanding pilot-scale and industrial scale photoreactors were successfully implemented, namely the "full-scale solar PWT operating in Cali, Columbia" [15, 20] or at the pilot-scale photoreactor at the solar platform in Almeria [21].

## **Photocatalytic microreactors with applications in wastewater treatment**

Micro-photoreactors are defined as miniaturized systems where the advantageous features of microfluidic devices are incorporated into the conventional photocatalytic reactors [22]. The increased reaction rate due to the high surface to volume ratio [23-25], short diffusion distance [23] (i.e., 10-100  $\mu\text{m}$  [24]), short reaction time [26], operating regime with negligible mass transfer limitations [26], and the relatively uniform light distribution [27] are the promising characteristics of photocatalytic micro-photoreactors which differentiate them apart of conventional photocatalytic reactors. In addition to this, self-refreshing effect [24], and the multiple functionalities (i.e., micro-mixing) of the microreactors must be considered [24].

A suggested classification of microreactors (MRs) used for photocatalytic wastewater treatment distinguishes (i) capillary (single or multi-capillary), (ii) single- and multi-channel, (iii) planar and (iv) multiphase MRs [28]. Among these, multiphase microreactors have considerable importance in photocatalytic wastewater treatment due to the requirement of  $\text{O}_2$  for the photooxidation of organic molecules [29]. Therefore, the presence of GLS phases is highly desired. Among the multiphase microreactors, falling film microreactors (FFMRs) are considered as one of the most promising micro-structured devices for the conduction of GLS photocatalytic reactions [14, 30] with continuous contacting of the phases [31]. Both gravity

and the microchannels have contribution in stabilizing the liquid film [32]. FFMR with parallel straight channels embedded in a plate, FFMR with parallel channels embedded in a cylinder, and FFMR with a single helical channel on a cylinder are the well-known FFMR configurations [33]. The conduction of heterogeneous photocatalytic reactions in FFMR can be performed in two ways: either *via* coated microchannels [34] or slurry reaction mixture [35]. Further information about the working principle of this type of reactor will be presented in the scientific contribution sections (2.4) and (2.5).

### **Selected aspects of the mathematical modeling of photoreactors**

Mathematical models are extremely important for scaling-up of photoreactors. The sub-models integrated into the modelling of photoreactors are the fluid dynamic model, the radiation absorption-scattering model, the radiation emission model, and the kinetic model [15, 36]. The equations of the sub-models can be solved either coupled or uncoupled [15], however the uncoupled solving approach is possible only if certain conditions are fulfilled. In the PhD thesis selected aspects related to the mathematical modelling of photoreactors are presented.

## General and specific research objectives

As it was already highlighted in the previous section of this thesis, heterogeneous photocatalysis has opened new perspectives into environmental depollution. This work may provide potential solutions *via* heterogeneous photocatalysis for the problems of unsatisfactory quality of drinking water and increasing atmospheric CO<sub>2</sub> concentration. The three pillars of heterogeneous photocatalysis, i.e., catalysts, photoreactors and process engineering, are integrated into this PhD thesis. Therefore, this work is composed of two main parts. While in the first part different approaches targeting the enhancement of selected photocatalysts are presented, in the second part the investigations related to the studied photoreactors and on (micro) reaction engineering aspects are discussed. Therefore, two general research objectives and further specific research objectives were formulated, as presented below.

**General research objective no. 1:** Development of efficient alkaline earth metal titanate-based catalysts (CaTiO<sub>3</sub> and SrTiO<sub>3</sub>-based) for photocatalytic applications.

The development of efficient photocatalyst is required for the conduction of photocatalytic processes. Since two perovskite-type catalysts were studied, two specific research objectives (SO1.1 and SO1.2) were proposed within this section, as given below.

**SO1.1:** Optimization of the photocatalytic efficiency of hydrothermally synthesized CaTiO<sub>3</sub> for rhodamine B degradation with the aid of mathematical models

1. Design of the hydrothermal syntheses of CaTiO<sub>3</sub> *via* Box Behnken design.
2. Implementation of the synthesis procedures of CaTiO<sub>3</sub> according to the chosen experimental design, followed by the assessment of photocatalytic efficiency.
3. Implementation of different empirical mathematical models based on the experimental data.
4. Empirical model-based optimization of the photocatalytic efficiency of CaTiO<sub>3</sub> for rhodamine B degradation.

**SO1.2:** Enhancement of photocatalytic efficiency of SrTiO<sub>3</sub> *via* trial-and-error approach and strategic design principles for photocatalytic CO<sub>2</sub> reduction

1. Design of the SrTiO<sub>3</sub>-based (SrTiO<sub>3</sub>-SrCO<sub>3</sub>) support *via* trial-and-error approach aiming the control of SrCO<sub>3</sub> content.
2. Further modification of the support aiming the enhancement of the efficiency, and the control of the selectivity towards the generation of a certain solar fuel.
3. Assessment of photocatalytic CO<sub>2</sub> reduction activity.
4. Establishment of structure-function correlations.

**General research objective no. 2:** Experimental and numerical characterization of flow in a multi-channel falling film microreactor and its application for kinetic studies of multiphase photocatalytic reaction.

Conduction of photocatalytic multiphase reactions in microreactors is very promising, due to the promising features of the microfluidic devices. However, regardless to the intensive investigations, there are still a lot of open questions targeting phenomenological aspects.

Therefore, this thesis may provide answers for certain questions regarding to the multiphase flow behavior and kinetics, as given in the specific research objectives (SO2.1 and SO2.2).

**SO2.1.** Experimental and numerical assessment of multiphase flow behavior in an open channel falling film microreactor prototype.

1. Evaluation of the flow distribution and hydraulic residence time in the single (coated/uncoated) microchannels *via* tracer experiments using different solvents (ethanol, water).
2. Evaluation of the capillary effects in the microreactor.
3. Assessment of the influence of selected parameters (flow rate, plate inclination angle, GLS contact angle) on the flow behavior (i.e., flow stability, mean film thickness).
4. Establishment of correlations.

**SO2.2.** Photocatalytic antibiotic degradation in coated open microchannels by applying 2D and 3D flow modeling with kinetics.

1. Assessment of the operating regime of the photoreactor.
2. Evaluation of the external and internal mass transfer limitations *via* empirical and experimental methods.
3. Implementation of 2D and 3D model of the coupled momentum and mass balance equations.
4. Fitting of the kinetic parameters.

## Chapter 2. Scientific Contributions

### (2.1) Experimental data-driven and phenomenological modeling approaches targeting the enhancement of CaTiO<sub>3</sub> photocatalytic efficiency<sup>†</sup>

#### 1. Introduction

The development of highly efficient photocatalysts can be considered a promising alternative for solving the environmental concern related to the improper or low treatment effectiveness of wastewaters. Recently, alkaline earth metal titanates (i.e., CaTiO<sub>3</sub>, SrTiO<sub>3</sub>, BaTiO<sub>3</sub>) have attracted considerable interest in the field of photocatalysis [37]. Due to their promising band structure [37] they can be used to degrade dyes [38-40], to produce hydrogen [41-43], to reduce Cr<sup>6+</sup> in water (especially with SrTiO<sub>3</sub>, [44]), and to transform CO<sub>2</sub> into valuable products *via* photoreduction [45, 46].

The first part of this work offers an overview of the relationship between selected hydrothermal synthesis parameters and the photocatalytic efficiency of CaTiO<sub>3</sub> for RhB degradation *via* different modeling approaches. The second part provides an insight into the phenomenological interpretation of the photocatalytic efficiency. The proposed integrated approach of the photocatalyst synthesis, development of the data-driven modeling methodology in association with phenomenological interpretations and optimization of the synthesis condition for obtaining the highest photodegradation efficiency may be considered as the main and novel contributions of this work.

#### 2. Material and methods

*Chemicals.* The chemicals used for the hydrothermal synthesis of CaTiO<sub>3</sub> were as follows: Ca(NO<sub>3</sub>)<sub>2</sub>·4H<sub>2</sub>O (Lach-Ner, ≥99%), CaCl<sub>2</sub> (Chempur, analytically pure), NaOH (Chempur, analytically pure), Ti(C<sub>4</sub>H<sub>9</sub>O)<sub>4</sub> (Sigma-Aldrich, 97%), C<sub>2</sub>H<sub>6</sub>O (Merck Millipore, analytically pure). The degradation of RhB dye (C<sub>28</sub>H<sub>31</sub>ClN<sub>2</sub>O<sub>3</sub>) (ReAnal, analytically pure) in aqueous solution was studied in this work.

*Synthesis of CaTiO<sub>3</sub>.* The hydrothermal crystallizations were carried out under specified conditions (synthesis temperature – X<sub>1</sub>: 180, 190 or 200 °C, synthesis duration – X<sub>2</sub>: 20, 24 or 28 h, concentration of the shaping agent – X<sub>3</sub>: 0.670, 1.005 or 1.340 M, type of Ca<sup>2+</sup> precursor – X<sub>4</sub>: Ca(NO<sub>3</sub>)<sub>2</sub> or CaCl<sub>2</sub>) according to the chosen experimental design.

*Assessment of photocatalytic efficiency.* The photocatalytic efficiency was assessed in a cylindrical slurry-type photoreactor with external irradiation (6 × 6 W, λ<sub>max</sub> = 365 nm) for RhB degradation (C<sub>0</sub> = 10 μM). The samples were withdrawn at selected times (0, 0A, 30, 60, 120, 180, 240 min), followed by their centrifugation, filtration and analysis *via* an Analytic Jena Specord 250 Plus UV–vis spectrophotometer.

---

<sup>†</sup> Bı́orka Boga, Vasile-Mircea Cristea, Istvan Szekely, Felix Lorenz, Tamas Gyulavari, Lucian Cristian Pop, Lucian Baia, Zsolt Pap, Norbert Steinfeldt, and Jennifer Strunk, Experimental data-driven and phenomenological modeling approaches targeting the enhancement of CaTiO<sub>3</sub> photocatalytic efficiency, *Sustainable Chemistry and Pharmacy*, **2023**, 33, 101045 (DOI: 10.1016/j.scp.2023.101045)

*Experimental design.* The Box-Behnken experimental design (BBD) was specifically applied for two approaches, according to the type of  $\text{Ca}^{2+}$  precursor, i.e. either  $\text{Ca}(\text{NO}_3)_2$  or  $\text{CaCl}_2$  ( $X_4$ ), and for three continuous factors ( $X_1, X_2, X_3$ ) with three levels (low: -1, center: 0, high: +1)

**Table 1.** Experimental range and levels of independent variables

No.	Continuous factor	Low level (-1)	Center level (0)	High level (+1)
1.	$X_1$ ( $^\circ\text{C}$ )	180	190	200
2.	$X_2$ (h)	20	24	28
3.	$X_3$ (M)	0.670	1.005	1.340
	Categorical factor	0	1	
4.	$X_4$	$\text{Ca}(\text{NO}_3)_2$	$\text{CaCl}_2$	

*Regression analysis.* A second-order model was chosen to describe the relationship between the independent variables and the conversion, The individual and the interaction effects between the variables were evaluated by employing analysis of variance (ANOVA) using Minitab v18 [47].

*Artificial neural network models.* Feedforward backpropagation artificial neural network models (FB-ANNs) were implemented in MATLAB software environment to predict the photocatalytic efficiency for given inputs.

*Assessment of morpho-structural and optical peculiarities of the synthesized catalysts.* The following equipment were used for the morpho-structural and optical characterization of the samples: a Shimadzu 6000 diffractometer (Shimadzu Corporation, Kyoto, Japan) equipped with a  $\text{Cu-K}\alpha$  source ( $\lambda = 1.54 \text{ \AA}$ ), a FEI Quanta 3D FEG scanning electron microscope (SEM) (accelerating voltage 25 kV), a NOVAtouch (Quantachrome Instruments), a JASCO-V650 spectrophotometer equipped with an ILV-724 integration sphere.

*Kinetic modeling.* The first step within the kinetic modeling assumed the determination of pseudo-first order reaction rate constant, considering the Langmuir Hinshelwood kinetic model [48, 49].

Furthermore, a validated two-dimensional mathematical model of a slurry photoreactor provided by Palmisano and coworkers [50] was used to determine the rate constants for substrate adsorption ( $k_{\text{ads}}$ ), desorption ( $k_{\text{des}}$ ) degradation ( $k_{\text{degr}}$ ) and intensity exponent ( $\alpha$ ) *via* optimization (least-square method).

### 3. Results and discussion

#### 3.1. Effect of synthesis conditions on photocatalytic efficiency

To establish a relationship between the synthesis conditions ( $T - X_1, t - X_2, C - X_3$ ) and the photocatalytic efficiency (expressed *via* conversion  $X$ ), the first 30 sets of synthesis were carried out according to the BBD. They were followed by photocatalytic tests (as described in the methods section). The most efficient photocatalyst ( $X = 79.4 \%$ ) within the designed experiments was synthesized using  $\text{CaCl}_2$  as a  $\text{Ca}^{2+}$  source (denoted R2) and 0.67 M NaOH (C), which were subjected to hydrothermal treatment for 24 h (t) at 200  $^\circ\text{C}$  (T). The least efficient

photocatalyst was synthesized using  $\text{Ca}(\text{NO}_3)_2$  as a  $\text{Ca}^{2+}$  source (denoted R1) and 1.34 M NaOH (C), with treatment at 180 °C (T) for 24 h (t). The latter case showed the degradation of only 20.4 % of the pollutant.

Two data-driven models, that is, polynomial regression (3.1.1.) and FB-ANNs (3.1.2.), were implemented to establish correlations between the hydrothermal synthesis conditions of  $\text{CaTiO}_3$  photocatalysts and their photocatalytic efficiency.

### 3.2. Polynomial model fitting and ANOVA

Considering the categorical input variable ( $X_4$ , that is, the type of  $\text{Ca}^{2+}$  precursor), two separate polynomial models were implemented for describing the continuous factors influence on conversion ( $Y_1, Y_2=f(X_1, X_2, X_3)$ , R1  $\text{Ca}(\text{NO}_3)_2$ , R2  $\text{CaCl}_2$ ). As a first approach, full quadratic second-order models were fitted by involving all the linear ( $X_1, X_2, X_3$ ), square ( $X_1^2, X_2^2, X_3^2$ ) and interaction ( $X_1X_2, X_1X_3, X_2X_3$ ) terms. All predicted coefficients were estimated *via* the least-squares method. The pre-exposed significance ( $\alpha$ ) level was chosen to be 0.05. Because the p-value associated to certain terms from the full quadratic models were found to be statistically not significant ( $p>0.05$ ), these models were refitted without those terms.

$$Y_{R1} = 881.3 - 26.27 \cdot X_2 - 972 \cdot X_3 - 1.58 \cdot 10^{-2} \cdot X_1^2 + 0.15 \cdot X_2^2 + 92.64 \cdot X_3^2 + 8.94 \cdot 10^{-2} \cdot X_1 \cdot X_2 + 3.58 \cdot X_1 \cdot X_3 + 2.60 \cdot X_2 \cdot X_3 \quad (1)$$

$$Y_{R2} = 1243 - 15.55 \cdot X_1 + 32.64 \cdot X_2 - 264.9 \cdot X_3 + 4.22 \cdot 10^{-2} \cdot X_1^2 - 0.69 \cdot X_2^2 + 110.66 \cdot X_3^2 \quad (2)$$

The comparison between the experimentally determined and model-predicted conversion values is presented in Figure 2.

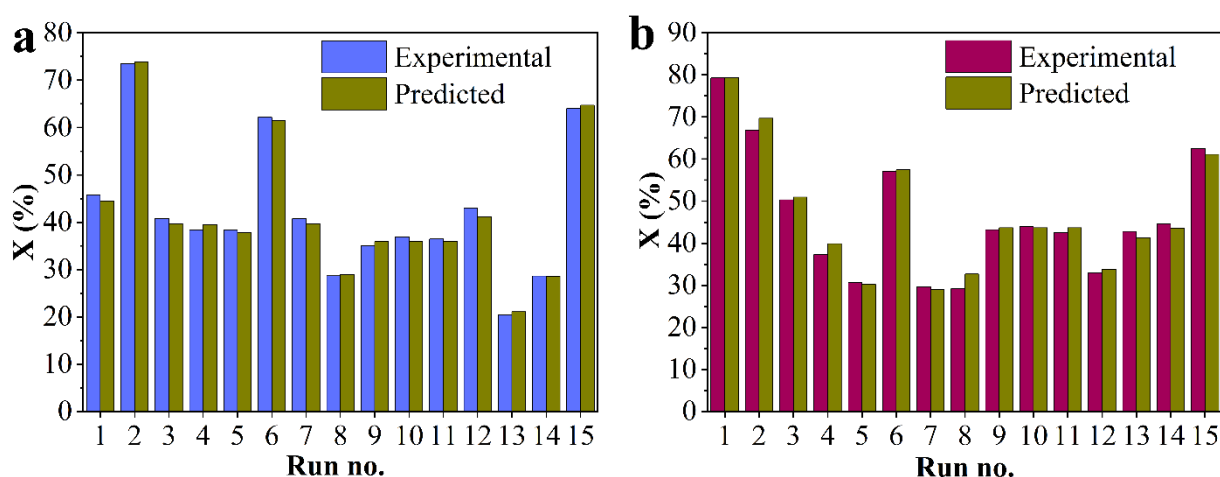


**Figure 2.** Comparison between experimentally determined and model-predicted conversion values: a. R1, b. R2

The results presented showed that all three selected synthesis parameters have a significant effect on the photocatalytic performance of  $\text{CaTiO}_3$ . Considering the second-order regression

models developed in this work, optimization of the conversion was carried out *via* the Optimization Toolbox (optimtool) of MATLAB 2015b. Both SQP (fmincon solver) and genetic algorithm were used for finding the maximum conversion and the corresponding synthesis conditions (T, t, C), within the predefined ranges of the decision variables (T: 180–200 °C, t: 20–28 h, C: 0.67–1.34 M). The optimal synthesis conditions were determined to be 180 °C, 20 h and 0.67 M for R1, and 200 °C, 23.67 h and 0.67 M for R2. The new experiments using the synthesis conditions proposed by optimization showed at this points a conversion of 66 % (R1) and of 95.7 % (R2). Considering the experimental and model-predicted maximum conversion values, their difference was attributed to the limitations of the chosen experimental design (BBD) that involved a parsimonious number of experiments. The under- and overestimated conversion was assumed to occur due to the lack of experimental data at the extreme points (180 °C, 20 h, 0.67 M) and in intermediate position (200 °C, 23.7 h, 0.67 M) used for model implementation (as can also be observed in Table 2). However, for R2 (i.e., when CaCl<sub>2</sub> was applied as Ca<sup>2+</sup> source), the model-based investigations led to the identification of the optimized synthesis conditions under which experimentally confirmed maximum photocatalytic efficiency was assessed.

### 3.3. Artificial neural network models

Due to the relatively small data set (26 input–output pairs), the architecture of the trained network was structured as follows: one input, one hidden and one output layer (Figure 3). While the number of input and output neurons was fixed (i.e., four input neurons: synthesis temperature – X<sub>1</sub>, synthesis duration – X<sub>2</sub>, concentration of shaping agent – X<sub>3</sub>, type of Ca<sup>2+</sup> source – X<sub>4</sub>, 1 output neuron: conversion – X), the number of hidden neurons, activation functions and training functions were selected by repeated experimentally conducted training tests.

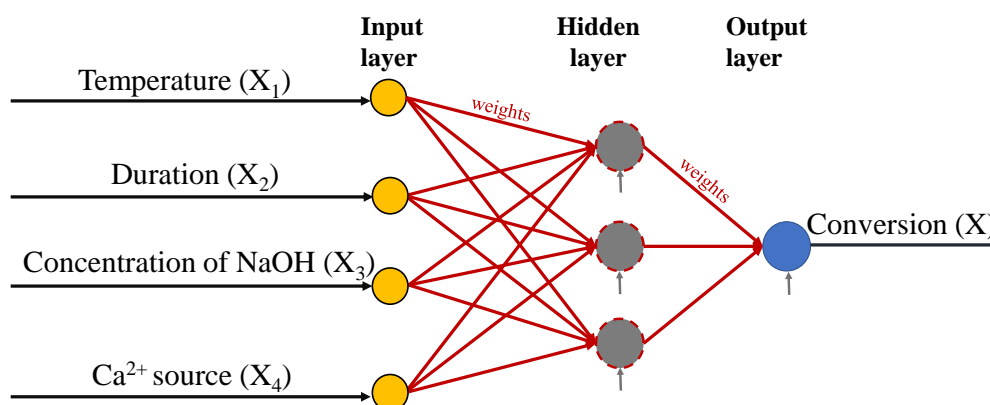


**Figure 3.** The architecture of the trained ANN with a maximum number of hidden neurons

According to the parameters described above, the most efficient FB-ANN architecture was obtained when three hidden neurons, the tangent sigmoid (tansig) transfer function, and the trainoss learning algorithm were used. In this case the determined correlation coefficient for testing was 0.97 ( $R_{\text{test}}$ ), and the mean relative error for testing was 8.80% ( $\Delta\epsilon_{r,\text{mean,test}}$ ).

An optimization procedure was also performed by employing the most efficient FB-ANN that we designed. The maximum photocatalytic efficiency (76.2%) was predicted when the following synthesis conditions were applied: 180 °C ( $X_1$ ), 20 h ( $X_2$ ), 0.67 M ( $X_3$ ) and  $\text{Ca}(\text{NO}_3)_2$  ( $X_4$ ) as the  $\text{Ca}^{2+}$  source. The optimal synthesis conditions determined in this way overlap with the results from the optimization step based on polynomial regression models. The limitation of the chosen experimental design (i.e., lack of experimental data at the extreme points) was also highlighted in this case.

### *3.4. Correlations between the morphological, structural, textural, optical properties of the designed $\text{CaTiO}_3$ samples and their photocatalytic activity*

The main aim of this work was to highlight the relationship between synthesis parameters and photocatalytic efficiency, and between morpho-structural particularities and photocatalytic efficiency by using different modeling approaches. However, this study also provides a brief overview on the cause–effect relationship between the synthesis conditions and morpho-structural particularities of  $\text{CaTiO}_3$ .

The type of  $\text{Ca}^{2+}$  precursor can have a considerable impact on the morphological, structural, optical and photoelectrochemical properties of the studied material. To investigate the effect of the  $\text{Ca}^{2+}$  precursor on morphological and structural properties, SEM micrographs of the samples synthesized according to the central point design (CE, 190 °C, 24 h, 1 M) were compared. Considering the SEM micrographs, two distinct types of morphology were observed: microrods and square-shaped particles that were not well-defined. Their ratio and arrangement differed for each sample. CE1 had a layered structure, which assured a more ordered aspect for this sample, in comparison to CE2.

Synthesis temperature can have a considerable effect on the morphology [51] and surface features of perovskites [52]. To investigate this aspect for our  $\text{CaTiO}_3$  samples (i.e., on their specific surface area, SSA), the SSAs of certain pairs of samples (from R1) were compared. In certain cases, considerably higher SSAs were observed for samples synthesized at a higher crystallization temperature (200 °C). However, in other cases, this trend could not be observed. This result was expected because of the interaction effects between the input variables.

The duration of hydrothermal treatment determines the degree of crystallinity [53]. According to the literature, enhanced charge transfer (from the center to the surface) and improved photocatalytic activity were observed for highly crystalline samples [54]. All of reflections identified in the XRD pattern of the studied samples were assigned to the orthorhombic  $\text{CaTiO}_3$  phase (JCPDS No. 22-0153) [55]. Based on the qualitative analysis of XRD patterns, no significant differences were identified between the samples.

Finally, it is possible to adjust the growth rates of selected crystallographic planes by changing the concentration of a suitable shaping agent [56]. The lowest predefined shaping agent concentration resulted in the desired photocatalytic feature.

### 3.5. Kinetic modeling

To investigate the photodegradation of RhB, a set of kinetic parameters (pseudo-first order reaction rate constant –  $k_{obs}$ , reactant adsorption rate constant –  $k_{ads}$ , absolute kinetic constant –  $k_{degr}$ , desorption rate constant –  $k_{des}$ , light intensity exponent –  $\alpha$ ) were determined using the mathematical model implemented and validated by Palmisano and coworkers [50]. Understanding the terms linked to the adsorption constant ( $K_{ads}$ ) has a pivotal role in obtaining an overview on the surface reaction kinetics.

The first step within the kinetic modeling was related to the evaluation of kinetic data considering the Langmuir–Hinshelwood mechanism. The next step was related to the calibration of the kinetic parameters based on optimization. The aim of the optimization problem was to minimize the square difference between the theoretical calculated and experimental data-based obtained pseudo-first order reaction rate constant.

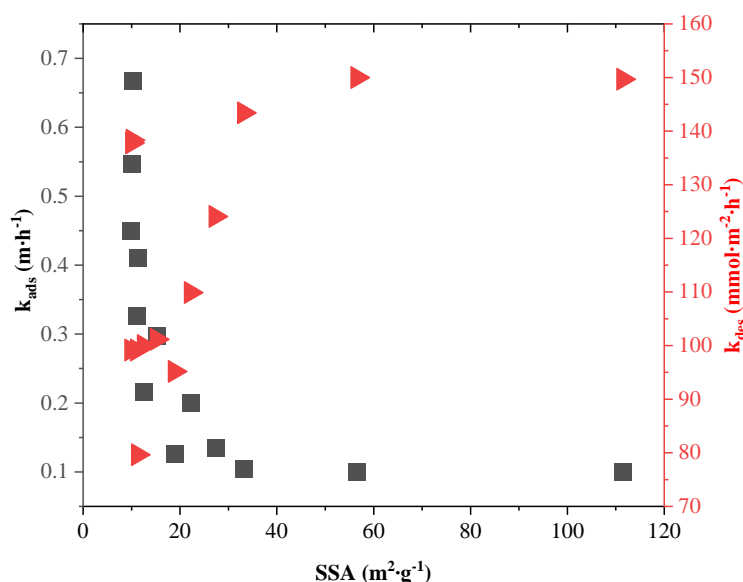


**Figure 4.** Correlation between specific surface area (SSA) and the computed adsorption, desorption kinetic constants ( $k_{ads}$ ,  $k_{des}$ ) in the case of R1

The computation of  $k_{obs}$  assumed the calculation of a double integral, as given in the main text of the manuscript.

The fitted  $k_{ads}$ ,  $k_{des}$  values were correlated with SSA. This is presented in Figure 4. While the  $k_{ads}$  values were situated between 0.10-0.67 m·h<sup>-1</sup>, the  $k_{des}$  had the values varying in the range of 79 - 150 mmol·m<sup>-2</sup>·h<sup>-1</sup>. According to Figure 8, it can be observed that a higher SSA led to lower  $k_{ads}$  and higher  $k_{des}$ . The reason for this correlation relies on the relationship between SSA, surface tension and rate of adsorption/desorption processes. While low SSA is associated with high surface tension (and implicitly high adsorption rate – high  $k_{ads}$ ), high SSA is linked to low surface tension (high desorption rate – high  $k_{des}$ ) [57]. Furthermore, the formation of intermediates during degradation (and adsorbed on the surface of the catalyst) can influence on the rate of surface processes (adsorption-desorption).

#### 4. Conclusions

The present work highlighted that the appropriate selection of synthesis conditions could improve the photocatalytic activity of the hydrothermally obtained  $\text{CaTiO}_3$ . Second-order polynomial regression and artificial neural network models were applied to establish correlations between selected synthesis parameters ( $T$ ,  $t$ ,  $C_{\text{NaOH}}$ ,  $\text{Ca}^{2+}$  precursor type) and conversion values for rhodamine B photodegradation, which were further used for optimization. Thirty hydrothermal syntheses were performed according to the Box-Behnken design, followed by the assessment of photocatalytic performance (20-80 % conversion). Considering the most favorable synthesis conditions determined from optimization (200 °C, 23.7 h, 0.67 M,  $\text{CaCl}_2$  precursor), the photocatalytic efficiency of the subsequently synthesized and experimentally validated  $\text{CaTiO}_3$  catalyst was ~96%. To overview the morphological, structural, and optical peculiarities, selected  $\text{CaTiO}_3$  samples were analyzed by complementary methods (i.e., SEM: square-shaped particles, XRD: orthorhombic crystal phase,  $\text{N}_2$  sorption – SSA: 10-120  $\text{m}^2\cdot\text{g}^{-1}$ , DRS –  $\Delta E_g$ : 3.5-3.6 eV). Finally, specific kinetic parameters (i.e., adsorption –  $k_{\text{ads}}$ : 0.10-0.67  $\text{m}\cdot\text{h}^{-1}$  and desorption constant –  $k_{\text{des}}$ : 79 - 150  $\text{mmol}\cdot\text{m}^{-2}\cdot\text{h}^{-1}$ , absolute kinetic rate constant –  $k_{\text{degr}}$ : 0.001-0.01  $\text{mmol}\cdot\text{m}^{-2(1-\alpha)}\cdot\text{W}^{-\alpha}\cdot\text{h}^{-1}$ ) were determined using a validated mathematical model from the literature considering the Langmuir-Hinshelwood mechanism and the pseudo-steady state assumptions. The following conclusions were deduced based on the kinetic modeling: (1) the higher the photocatalytic activity, the higher the absolute kinetic rate constant was; (2) with increasing specific surface area the rate of adsorption decreased and that of desorption increased.

## (2.2.) Role of SrCO<sub>3</sub> on photocatalytic performance of SrTiO<sub>3</sub>-SrCO<sub>3</sub> composites<sup>‡</sup>

### 1. Introduction

Titanium-based materials, such as titania, alkaline earth metal titanates, etc., are considered as suitable candidates for photocatalytic applications [37, 58]. Among these, SrTiO<sub>3</sub> seems to be a promising candidate given its band-structure [59], long lifetime of the photogenerated charge carriers, considerable catalytic activity, chemical and thermal stability [60]. One unique property of SrTiO<sub>3</sub> is directly related to its slightly different conduction band (CB) edge situated at a more negative potential in comparison to anatase (i.e.,  $E_{CB}(\text{anatase})$ : -0.1 V,  $E_{CB}(\text{SrTiO}_3)$ : -0.3 V vs. NHE at pH=0 [61]), which has a direct influence on its water splitting ability. While the CB position of TiO<sub>2</sub> (both anatase and rutile) does not allow the efficient H<sub>2</sub> production (from H<sub>2</sub>O) unless in the presence of co-catalysts, this limitation is overcome in the case of SrTiO<sub>3</sub> [62, 63].

In this work SrTiO<sub>3</sub>-SrCO<sub>3</sub> composites with different SrCO<sub>3</sub> content were synthesized and applied for DCFNa photodegradation and CO<sub>2</sub> photoreduction. Preliminary purification of KOH in association with the conduction of synthesis in Schlenk line technique, excess of Sr<sup>2+</sup> source, and different Ti<sup>4+</sup> sources (i.e., anatase vs. P25) were applied aiming the control of SrCO<sub>3</sub> content of SrTiO<sub>3</sub>-based catalysts. According to our best knowledge, the combination of preliminary purification of KOH with Schlenk line technique, and the application of different Ti<sup>4+</sup> precursors for the adjustment of SrCO<sub>3</sub> content of the SrTiO<sub>3</sub>-based catalysts have not been reported yet in the scientific literature. It is demonstrated that the presence of SrCO<sub>3</sub> both increases the DCFNa degradation as well its mineralization. Furthermore, some reasons for the higher activity of SrTiO<sub>3</sub>-SrCO<sub>3</sub> compared to SrTiO<sub>3</sub> are discussed.

### 2. Experimental

*Chemicals.* Strontium nitrate (Sr(NO<sub>3</sub>)<sub>2</sub>, ≥99%, Sigma Aldrich), titanium (IV) oxide - anatase (TiO<sub>2</sub>, 99.5%; IoliTec), titanium (IV) oxide – P25 (TiO<sub>2</sub>, 99.9%, Evonik), potassium hydroxide (KOH, ≥85%, Sigma Aldrich), ethanol (C<sub>2</sub>H<sub>6</sub>O, >99%, Merck), ammonium oxalate monohydrate ((NH<sub>4</sub>)<sub>2</sub>C<sub>2</sub>O<sub>4</sub>·H<sub>2</sub>O, ≥99%, Sigma Aldrich), p-benzoquinone (C<sub>6</sub>H<sub>4</sub>O<sub>2</sub>, >98%, Sigma Aldrich), isopropanol (C<sub>3</sub>H<sub>8</sub>O, 99.9%, Merck), terephthalic acid (C<sub>8</sub>H<sub>6</sub>O<sub>4</sub>, >98%, Merck), 5,5-dimethyl-1-pyrroline-N-oxide (C<sub>3</sub>H<sub>11</sub>NO, >98%, Enzo Life Sciences GmbH). Commercial strontium titanate (SrTiO<sub>3</sub>, 99.9%, IoliTec) and strontium carbonate (SrCO<sub>3</sub>, 99.9%, Sigma Aldrich) were used as reference catalysts. The chemicals for synthesis and analysis were used without any preliminary purification except for KOH.

#### *Material synthesis*

The synthesis of SrTiO<sub>3</sub>-based catalysts with different SrCO<sub>3</sub> content (5, 15, 21, 24 wt%) was carried out *via* hydrothermal treatment (180 °C, 12 h), followed by washing (once with ethanol, three times with distilled water) and drying (80 °C, 12 h).

---

<sup>‡</sup>Biborka Boga, Norbert Steinfeldt, Nikolaos G. Moustakas, Tim Peppel, Henrik Lund, Jabor Rabeah, Zsolt Pap, Vasile-Mircea Cristea, Jennifer Strunk, Role of SrCO<sub>3</sub> on photocatalytic performance of SrTiO<sub>3</sub>-SrCO<sub>3</sub> composites, *Catalysts*, **2022**, 12(9), 978, (DOI: 10.3390/catal12090978)

The "starting" synthesis (STO\_15\_SCO) involved the addition of  $\text{Sr}^{2+}$  and  $\text{Ti}^{4+}$  precursors into 70 mL  $\text{H}_2\text{O}$  in stoichiometric ratio, thus obtaining an initial reaction mixture with 0.083 M  $\text{Sr}(\text{NO}_3)_2$  and anatase (i.e. 1.270 g  $\text{Sr}(\text{NO}_3)_2$ , 0.479 g  $\text{TiO}_2$ ).

STO\_5\_SCO. Although the same initial precursor concentrations were achieved as in the previous case (i.e. 0.083 M  $\text{Sr}(\text{NO}_3)_2$  and  $\text{TiO}_2$  (anatase), 8 M KOH), in this case the hydrothermal treatment was performed under Schlenk line and at a lower scale ( $V_{\text{autoclave}}=47$  mL,  $V_{\text{reaction mixture}} = 30$  mL), given by the complexity of this approach.

The synthesis of STO\_21\_SCO was performed as the "starting" synthesis (i.e. STO\_15\_SCO) with the exception that the initial  $\text{Sr}^{2+}:\text{Ti}^{4+}$  molar ratio was 1.250:1.

The difference in the case of STO\_24\_SCO (vs starting synthesis) was related to the usage of P25 as  $\text{Ti}^{4+}$  precursor (instead of pure anatase).

### *Characterization*

The following equipment were used for the morpho-structural and optical characterization of the samples: a Merlin VP compact device (Zeiss, Oberkochen, Germany), an Xpert Pro diffractometer (Panalytical, the Netherlands) using  $\text{CuK}\alpha 1\text{K}\alpha 2$  radiation ( $\lambda_1=0.15406$  nm,  $\lambda_2=0.15443$  nm), a Lambda 650 spectrophotometer (Perkin Elmer, Waltham, MA, USA), a NOVAtouch (Quantachrome Instruments) a Netzsch STA 449 F3 Jupiter device.

### *Assessment of photocatalytic efficiency*

The photodegradation experiments took place in a double jacket glass cylindrical batch photoreactor ( $V\sim 120$  mL, Hassa labor). The suspension was irradiated with a Xe arc lamp (300 W) equipped with a reflector system (LOT Quantum Design). The irradiation of the reaction mixture was carried out from the top, where the distance between the reactor and reflector system was 6 cm. The light intensity inside of the reactor (at 8 cm distance from the reflector system) was  $625 \text{ mW}\cdot\text{cm}^{-2}$ . The DCFNa transformation was followed by High-Performance Liquid Chromatography (HPLC). The mineralization efficiency was assessed after 4 hours by evaluating the total organic carbon content (TOC) of the filtered (20  $\mu\text{m}$ ) reaction mixture. The dissolved carbonate content from the  $\text{SrTiO}_3$ -based catalyst was quantified *via* the inorganic carbon content of the reaction mixture (IC) using TOC analyser (multi N/C, 3100, Analytik Jena).

The same experimental conditions were assured during the scavenging experiments as during the degradation experiments using ammonium oxalate (AO), p-benzoquinone (PBQ), isopropanol (IPA). The initial concentration of scavengers in the reaction mixture was 393  $\mu\text{M}$  (AO, PBQ) and 1.57 mM (IPA).

The trapping of the hydroxyl radicals in the final reaction mixture was carried out according to method described by Marschall and coworkers [64].

The identification of the active species in the reaction mixture was performed *via in situ* Electron Paramagnetic Resonance (*in situ* EPR) measurements using 5,5-dimethyl-1-pyrroline-N-oxide (DMPO) as trapping agent. X-band-EPR spectra was recorded via Bruker EMX CW-micro EPR spectrometer.

The photocatalytic  $\text{CO}_2$  reduction activity of the selected  $\text{SrTiO}_3$ -based samples was assessed in high-purity gas phase photoreactor system described in detail by Mei and coworkers [65].

### 3. Results and Discussion

#### 3.1. Structure, morphology, surface and optical properties

The XRD powder patterns of the studied catalysts are presented in the main text of the manuscript. The commercially available SrTiO<sub>3</sub> (cSTO) was considered as the reference catalyst. The notation used for the hydrothermally synthesized samples is STO\_x\_SCO, where x represents the SrCO<sub>3</sub> content (5, 15, 21 and 24 wt%) of the samples determined *via* Rietveld analysis. Considerable differences were revealed in SrCO<sub>3</sub> content of the samples in function of the applied strategy (Table 2). As it was expected, the lowest SrCO<sub>3</sub> content (i.e., 5 wt%) was assessed when the alkaline reagent had undergone preliminary purification, and the synthesis was conducted under inert conditions. Furthermore, the primary crystallite size (PCS) of components is summarized in Table 2. While the PCS of SrTiO<sub>3</sub> was in the range of 18-28 nm, much higher values (49-57 nm) were obtained in the case of SrCO<sub>3</sub>.

**Table 2.** Summary of the applied strategy aiming the control of SrCO<sub>3</sub> content, the primary crystallite size (PCS) of components and the BET specific surface area for all tested photocatalysts

No	Sample	Strategy/Observation	PCS <sub>sto</sub> (nm)	PCS <sub>sco</sub> (nm)	SSA (m <sup>2</sup> ·g <sup>-1</sup> )	ΔE <sub>g</sub> (eV)
1	cSTO	--	28	--	15	3.23
2	STO_5_SCO	Preliminary purification of KOH and Schlenk line technique	18	49	16	3.18
3	STO_15_SCO	Starting synthesis	25	55	45	3.16
4	STO_21_SCO	r <sub>n</sub> (Sr <sup>2+</sup> :Ti <sup>4+</sup> ) = 1.25	20	54	33	3.18
5	STO_24_SCO	Modification of Ti <sup>4+</sup> source	19	57	41	3.16

The SEM micrographs of the selected SrTiO<sub>3</sub>-based samples are presented in the main text of the PhD thesis. No considerable morphological differences are revealed in the case of the selected samples. Two characteristic morphologies were identified, namely nanocubes and microrods (marked with white dotted line). While the length of these microrods was situated between 1-1.5 μm, their width was identified in the 165-400 nm range. The characteristic dimension of the nanocubes varied in the range of 40-80 nm, which are in agreement with the results reported in the literature [66].

The lowest specific surface area (BET-SSA) was assigned to the commercial SrTiO<sub>3</sub> (Table 2), because of its spherical morphology, which is characterized by the lowest surface area to volume ratio. Furthermore, relatively low SSA was determined in the case of

STO\_5\_SCO in comparison to the other hydrothermally synthesized samples (i.e., STO\_x\_SCO, where x: 15, 21, 24).

The absorption spectra of the studied samples were recorded in the UV-Vis range, as presented in the main text of the manuscript. The well-known procedure (i.e., extrapolation of the linear region of the Tauc plot) was applied, which led to  $\Delta E_g$  values situated in the range of 3.1-3.2 eV (Table 2), which agree with the values reported in literature. No considerable shift in the absorption edge can be observed in the case of samples with different SrCO<sub>3</sub> content in the recorded range, since SrCO<sub>3</sub> absorbs electromagnetic radiation characterized with relatively high energy (4.9 eV [67]), which cannot be resolved within the recorded range.

### 3.2. Photocatalytic results

#### 3.2.1. Photocatalytic diclofenac degradation

The photocatalytic activity of the SrTiO<sub>3</sub>-SrCO<sub>3</sub> was assessed by the degradation of DCFNa ( $C_0=25 \text{ mg}\cdot\text{L}^{-1}$ ) in aqueous solution under white light irradiation. The degradation curves are presented in Figure 5.a. 30 minutes were allocated for the establishment of adsorption-desorption equilibrium (stirring, dark) before turning on the light. Neglectable DCFNa adsorption can be observed on all the SrTiO<sub>3</sub>-based catalyst after the dark phase, which can be explained by the relatively low differences in SSA ( $15\text{-}45 \text{ m}^2\cdot\text{g}^{-1}$ ). The degradation of DCFNa was almost complete after 1 h irradiation in all studied samples (inclusively the commercial SrTiO<sub>3</sub> and SrTiO<sub>3</sub>-SrCO<sub>3</sub> composites). The degradation curve can be described by pseudo first-order kinetics as previously reported [68]. The fastest DCFNa degradation was achieved for STO\_5\_SCO and STO\_21\_SCO. Here, the rate constant was 4 times higher than that of pure SrTiO<sub>3</sub> (cSTO).

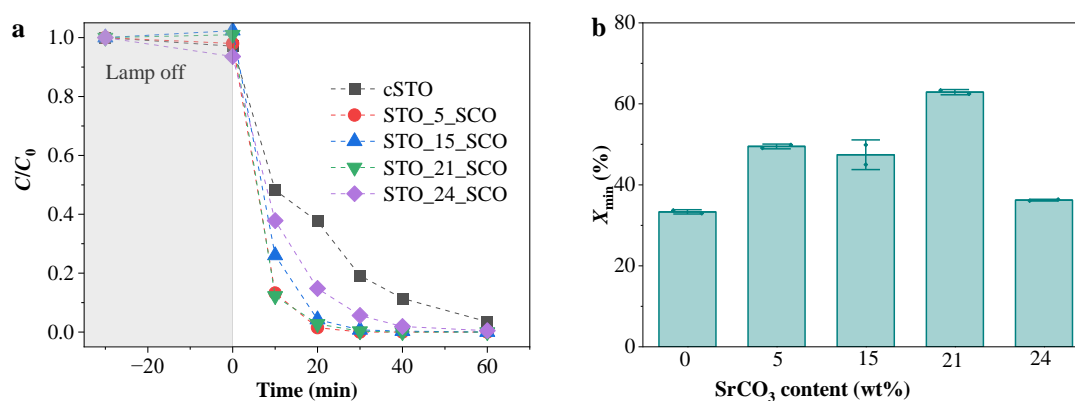


**Figure 5.** a. The degradation curves of DCFNa and b. The effect of SrCO<sub>3</sub> content on DCFNa mineralization after 4 h.

Beside DCFNa degradation, the effect of SrCO<sub>3</sub> content on mineralization was also investigated after 4 h. The mineralization of DCFNa during photolysis was below 3%, which agreed with previously reported results. According to Figure 5. b, higher mineralization efficiencies ( $X_{\min}$ ) were observed in samples containing SrCO<sub>3</sub> phase in comparison to cSTO. While quite similar mineralization efficiencies were assessed in the case of STO\_5\_SCO and

STO\_15\_SCO (~50%), the highest efficiency was reported in the case of STO\_21\_SCO (62%). Similar optimal SrCO<sub>3</sub> content (i.e., 19 wt%) of the SrTiO<sub>3</sub>-SrCO<sub>3</sub> catalyst was determined by Marquez-Herrera during the photodegradation of methylene blue [67].

To investigate whether the presence of SrCO<sub>3</sub> can influence the amount of reactive ·OH formed during irradiation, the terephthalic acid hydroxylation reaction was carried out using STO\_15\_SCO and cSTO (Figure 6.a). Considering the proportionality between concentration and photoluminescence (PL) intensity, the amount of ·OH were 3.5 × times higher in the reaction mixture using STO\_15\_SCO in comparison to cSTO. Since improved charge separation takes place in SrTiO<sub>3</sub>-SrCO<sub>3</sub> composites [69] (Figure 7), more holes are left over SrTiO<sub>3</sub>, which may lead to the formation of higher amount of ·OH. However, this is just evidence for the better charge separation, and not for the fact that ·OH are the main active species responsible for the photodegradation of DCFNa.

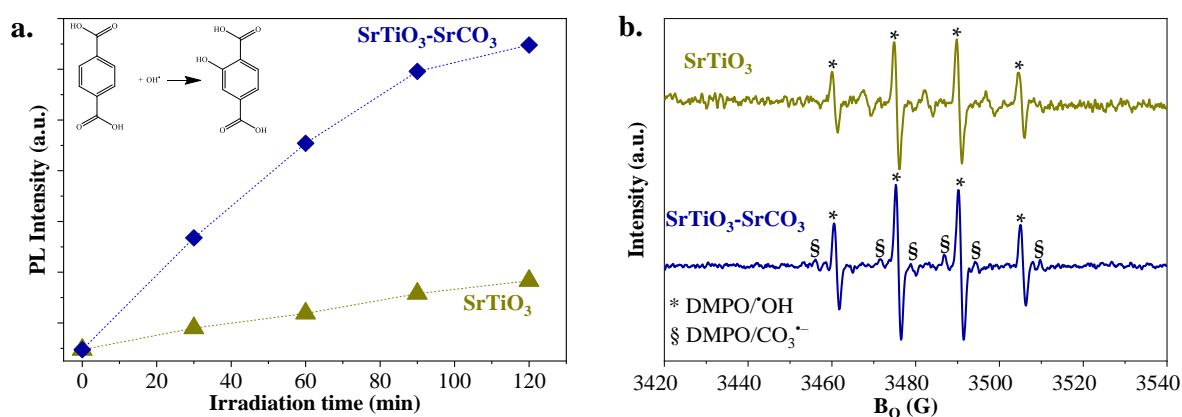


**Figure 6. a.** Time-dependent terephthalic acid hydroxylation in case of the cSTO and STO\_15\_SCO. **6.b.** *In situ* EPR spectra of the reaction mixture after the addition of DMPO in the presence of cSTO and STO\_15\_SCO.

Furthermore, to find out whether beside ·OH, further radicals were formed during the photocatalytic reaction, *in situ* EPR measurements were conducted with DMPO as trapping agent using cSTO and STO\_15\_SCO (Figure 6.b). Analyzing the *g* value (2.007) and the hyperfine splitting constants ( $a_N/a_H=1$ ), the DMPO/·OH adduct ( $a_N/a_H=1$  [70]) was identified in the reaction mixture when cSTO and STO\_15\_SCO was used (Figure 6.b). When STO\_15\_SCO was used signals of a second radical was observed additionally which can be assigned to the formation of a DMPO/CO<sub>3</sub><sup>•-</sup> adduct ( $a_N/a_H=1.37$  [70]).

### 3.2.2. Photocatalytic CO<sub>2</sub> reduction of SrTiO<sub>3</sub>-SrCO<sub>3</sub> in a high-purity gas-solid photoreactor

The STO\_15\_SCO and cSTO samples were evaluated within this section to get an overview on the photocatalytic CO<sub>2</sub> reduction activity of SrTiO<sub>3</sub>-SrCO<sub>3</sub> and SrTiO<sub>3</sub> samples. In the presence of CO<sub>2</sub> after 6 h of irradiation, the formation of 4.6 ppm and 1.6 ppm of CH<sub>4</sub> could be observed over cSTO and STO\_15\_SCO, as well as traces of C<sub>2</sub>H<sub>6</sub>.

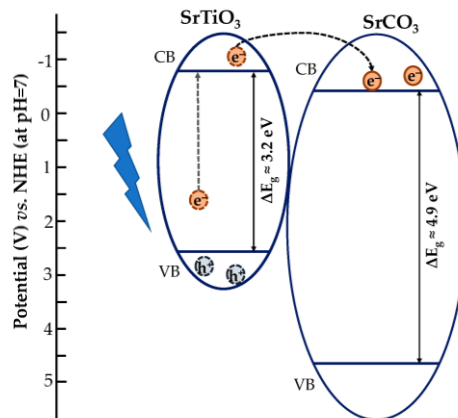


**Figure 7.** Scheme of the mechanism in SrTiO<sub>3</sub>-SrCO<sub>3</sub> [69, 71].

#### 4. Conclusion

This study shows different methods which can be applied to adjust the SrCO<sub>3</sub> content of hydrothermally synthesized SrTiO<sub>3</sub>. Similar primary crystallite size (of STO: 18-28 nm), band gap energy (3.16-3.23 eV) and specific surface area (15-45 m<sup>2</sup>·g<sup>-1</sup>) values were determined in the case of all studied SrTiO<sub>3</sub>-based samples with 5, 15, 21 or 24 wt% SrCO<sub>3</sub> content. Furthermore, the photocatalytic performance of SrTiO<sub>3</sub>-SrCO<sub>3</sub> catalysts was assessed in both oxidation (diclofenac mineralization) and reduction processes (CO<sub>2</sub> reduction).

Improved diclofenac mineralization (after 4 h) was determined in case of all SrTiO<sub>3</sub>-SrCO<sub>3</sub> (*vs.* SrTiO<sub>3</sub>) catalysts with an optimal SrCO<sub>3</sub> content of 21 wt% ( $X_{\text{mineralization}} = 62\%$ ). The enhanced mineralization of diclofenac using SrTiO<sub>3</sub>-SrCO<sub>3</sub> (*vs.* SrTiO<sub>3</sub>) may be explained by (1) the involvement of CO<sub>3</sub><sup>•-</sup> (*in situ* EPR), (2) better charge separation (and implicitly higher concentration of formed •OH), (3) favorable morpho-structural and surface properties (i.e., higher surface area). Finally, although higher CO<sub>2</sub> reduction activity was assessed for SrTiO<sub>3</sub> in comparison to SrTiO<sub>3</sub>-SrCO<sub>3</sub>, further investigations are required to clarify the involvement of SrCO<sub>3</sub>.

## (2.3.) Design of SrTiO<sub>3</sub>-Based Catalysts for Photocatalytic CO<sub>2</sub> Reduction <sup>§</sup>

### 1. Introduction

The photocatalytic conversion of CO<sub>2</sub> into valuable fuels (CH<sub>4</sub> or higher hydrocarbons) over metal oxide-based catalysts is a smart and promising solution for overcoming the problem of increasing atmospheric CO<sub>2</sub> concentration (425 ppm [4]) and energy demand [5].

In this work, the effect of NiO impregnation or/and Au-photodeposition on different SrTiO<sub>3</sub>-supports has been studied in association with the assessment of their photocatalytic CO<sub>2</sub> reduction activity and their light-induced CO<sub>2</sub> adsorption ability. As support, commercial SrTiO<sub>3</sub>, commercial SrCO<sub>3</sub>, and SrTiO<sub>3</sub>-SrCO<sub>3</sub> prepared by hydrothermal crystallization were employed. According to our best knowledge, the combination of the aforementioned components, namely NiO, Au, SrTiO<sub>3</sub> and SrCO<sub>3</sub> has not been previously studied in the literature. Additional motivating points of our work are related to the fact that, despite its potential, a relatively small number of studies are dealing with SrTiO<sub>3</sub>-SrCO<sub>3</sub> in photocatalytic CO<sub>2</sub> reduction applications [71] (it is mainly used for photooxidation of NO [69], CH<sub>4</sub> [72], and degradation of active pharmaceutical ingredients [73]), and that the effect of structural carbonates is still a matter of debate in photocatalytic CO<sub>2</sub> reduction (e.g., TiO<sub>2</sub> [74], ZnO [75]).

### 2. Experimental

#### *Chemicals*

The chemicals for synthesis and analysis: strontium nitrate (Sr(NO<sub>3</sub>)<sub>2</sub>, Sigma Aldrich, Germany, ≥99%), titanium(IV) oxide (anatase TiO<sub>2</sub>, 10-25 nm, Iolitec, Germany, 99.5%;), potassium hydroxide (KOH, Sigma Aldrich, Germany, ≥85%), nickel nitrate hexahydrate (Ni(NO<sub>3</sub>)<sub>2</sub>·6H<sub>2</sub>O, Merck, Germany, ACS), hydrogen tetrachloridoaurate (III) trihydrate (HAuCl<sub>4</sub>·3H<sub>2</sub>O, ABCR, Germany, 99.99%), ethanol (Merck, Germany, >99%), isopropanol (Merck, Germany, 99.9%). The chemicals for synthesis and analysis were used without any preliminary purification. The reference support materials were SrTiO<sub>3</sub> (Iolitec, Germany, 99.99%), SrCO<sub>3</sub> (Merck, Germany, 99.99%).

#### *Preparation of the studied materials*

The preparation of the studied materials included 3 steps, namely: (I) preparation of the support, (II) impregnation of the support with NiO, and Au photodeposition.

Optimized support: hydrothermally synthesized SrTiO<sub>3</sub>-SrCO<sub>3</sub> with ~ 18 wt % of SrCO<sub>3</sub> (STO-SCO (HT)). The synthesis of this heterojunction is described in our previous publication [73], with the specification that this case the initial ratio between the Sr<sup>2+</sup>: Ti<sup>4+</sup> precursors is 1.125.

Reference support: commercial SrTiO<sub>3</sub> (STO), commercial SrCO<sub>3</sub> (SCO) and the composite prepared from the commercial catalysts *via* the suspension method (i.e., STO-SCO (SM)).

---

<sup>§</sup> B borka Boga, Nikolaos G. Moustakas, Yunyan Han, Haijun Jiao, Carsten Kreyenschulte, Pawel Naliwajko, Thi Thanh Hoa Duong, Shuoping Ding, Anh Binh Ngo, Abdo Hezam, Tim Peppel, Vasile-Mircea Cristea, Norbert Steinfeldt, Jennifer Strunk, Design of SrTiO<sub>3</sub>-Based Catalysts for Photocatalytic CO<sub>2</sub> Reduction, Catalysis Science & Technology, 2024 (DOI: 10.1039/D4CY00313F)

Preparation of NiO/Support: The impregnation of the supports was done *via*  $\text{Ni}(\text{NO}_3)_2 \cdot 6\text{H}_2\text{O}$ , followed by calcination of the samples at 700 °C over 4 h. The nominal content of NiO was 0.3 wt%, which was in concordance to the experimentally determined  $\text{Ni}^{2+}$  content ( $\pm 5$  % relative error).

Au photodeposition: The Au-photodeposition was performed according to a method described previously [76]. The experimentally determined Au content (error  $\pm 10\%$ , theoretical Au content: 1 wt.%) of the samples was in concordance with the expected/theoretical Au content.

### *Material characterization*

The following methods were applied, namely: Inductively Coupled Plasma Optical Emission Spectroscopy (ICP-OES, Varian/Agilent 715-ES, Germany), Scanning Electron Microscopy (SEM, Merlin VP compact device Zeiss, Oberkochen, Germany), Scanning Transmission Electron Microscopy (STEM, ARM200F, Jeol, Tokyo, Japan), X-ray Diffraction (XRD, with  $\text{CuK}\alpha_1\text{K}\alpha_2$  radiation:  $\lambda_1=0.15406$  nm,  $\lambda_2=0.15443$  nm, Panalytical, the Netherlands), X-ray Photoelectron Spectroscopy (XPS, ESCALAB 2020IXL, Thermo Fischer Scientific), nitrogen sorption (NOVAtouch (Quantachrome Instruments), Diffuse Reflectance Spectroscopy (DRS, Lambda 650 spectrophotometer, Perkin Elmer), *in situ* Electron Paramagnetic Resonance Spectroscopy (*in situ* EPR, Bruker EMX CW-micro X-band EPR spectrometer), *in situ* Diffuse Reflectance Infrared Fourier Transformation Spectroscopy (*in situ* DRIFTS, Nicolet Protégé spectrometer equipped with a Harrick HVC DRP-5 cell and Praying Mantis mirrors), a high-purity gas-phase photoreactor system [77], first-principles methods – i.e., Density Functional Theory (and Density Functional Theory with the Hubbard U correction (Vienna ab initio simulation package, VASP).

## **3. Results and Discussion**

### *3.1. Structural features and properties*

The experimentally determined Au and  $\text{Ni}^{2+}$  contents ( $\text{Au}_{\text{exp}}$ ,  $\text{Ni}^{2+}_{\text{exp}}$ ) agreed with the theoretical values ( $\text{Au}_{\text{theo}}$ ,  $\text{Ni}^{2+}_{\text{theo}}$ ) based on the ICP-OES results (within an acceptable relative error range of  $\pm 10\%$ ), providing evidence about the efficiency of the impregnation and photodeposition processes.

The reflections of cubic  $\text{SrTiO}_3$  (ICDD 00-035-0734) and orthorhombic  $\text{SrCO}_3$  (ICDD 01-084-1778) phases were revealed in all XRD patterns of the STO-SCO (HT)-based samples (see in the main text of the manuscript). No additional reflections were identified in the case of NiO/STO-SCO (HT) sample (*vs.* STO-SCO (HT)) given by the relatively low loading of NiO on the support [78, 79]. Although no typical diffraction peaks of Au species (metal Au or  $\text{Au}_x\text{O}$ ) were expected in the recorded XRD patterns at such a low Au loading [80, 81], an additional relatively broad reflection can be observed at  $38.2^\circ$  ( $2\theta$ ) in the case of Au-STO-SCO (HT) and Au-NiO/STO-SCO (HT), which corresponds to the (111) plane of the face centered cubic Au-structure [82].

According to Rietveld analysis, the SCO content of the STO-SCO (HT)-based samples was 18 wt. %, which was in concordance with the carbonate-content calculated based on the carbon content of the samples (EA, 19 wt. %), indicating the crystallinity of SCO.

The Au-STO-SCO (HT) and Au-NiO/STO-SCO (HT) samples were analyzed *via* XPS. Based on the Ni 2p XP spectrum it can be concluded that mainly Ni<sup>2+</sup> species (binding energy of 855.56 eV), a small fraction of Ni<sup>3+</sup> species [83] might be also present (with binding energy of 857.90 eV), and that Ni<sup>0</sup> was not formed. Furthermore, the Au 4f XP spectra confirmed the presence of metallic Au. The XP spectra are presented in the Supplementary Material associated with this manuscript.

The morphological features of the studied samples were investigated by SEM, and STEM. SEM images of the selected (optimized) samples are presented in the main text of the manuscript. Two morphological entities can be revealed in the case of STO-SCO (HT)-based catalysts, namely nanocubes (STO) and isolated microrods (SCO). While the STO nanocubes have average particle sizes of 20-30 nm, the SCO microrods were 1.0-1.5  $\mu\text{m}$  in length with a diameter of ca. 150 nm. To have a closer look on the morphology and the contact between the components, STEM images, EDXS elemental maps and EDX spectra were recorded for the ternary composite, Au-NiO/STO-SCO (HT). The support shows rather cubic shaped SrTiO<sub>3</sub> particles which apparently have surface indentation or local pores according to the small darker areas. The high-resolution image then shows the NiO particle attached to such an SrTiO<sub>3</sub> support particle.

For an overview on the textural properties of the selected supports, the specific surface area (BET, SSA), the pore volume (BJH,  $V_P$ ) and the average pore size ( $r_P$ ) were assessed and summarized in the main text of the manuscript. The highest SSA can be observed for the STO-SCO (HT) sample, which may provide more CO<sub>2</sub> adsorption sites and facilitate the involvement of the adsorbed CO<sub>2</sub> in the subsequent surface reactions. As it was expected, the decrease of SSA was observed after sintering at 700 °C (i.e., from 52 m<sup>2</sup>·g<sup>-1</sup> for STO-SCO (HT) to 16 m<sup>2</sup>·g<sup>-1</sup> for NiO/STO-SCO (HT)), however this decrease was obvious only in the case of the hydrothermally synthesized support.

### 3.2. *Light absorption and electronic structure*

All the samples possess an absorption edge in the UV region (300-400 nm), highlighted in grey in the main text of the manuscript. The  $\Delta E_g$  of SrTiO<sub>3</sub> is determined, and it is equal to 3.2 eV. The determination of the  $\Delta E_g$  of SrCO<sub>3</sub> was not possible, since it cannot be resolved in the recorded range (200-800 nm). Moreover, considering the overlapping of the absorption edges in the recorded UV region (200-400 nm) and the low NiO loading, the determination of the NiO  $\Delta E_g$  is not possible based on the recorded spectra of the studied multicomponent systems. In the case of the Au-containing samples (i.e., Au-STO-SCO (HT), Au-NiO/STO-SCO (HT)), the plasmon resonance band is located at 540 nm, which is directly correlated to the Au NP size and shape [84].

### 3.3. *Unravelling the paramagnetic species under irradiation*

To reveal and clarify the presence of paramagnetic species under irradiation, serial recordings were performed under irradiation. Interestingly, in all studied samples a nearly isotropic signal was identified at  $g = 2.004$  ( $g_1 = g_2 = g_3$ ), which was assigned to the trapped electrons in oxygen vacancies (OVs) [85]. On the other hand, a relatively weak anisotropic signal was identified at 1.978, which may be assigned to the  $Ti^{3+}$  centers [85]. In case of the Au-containing samples (i.e., Au-STO-SCO (HT) and Au-NiO/STO-SCO (HT)), a relatively broad signal can be observed at  $g = 2.066$ , which can be correlated to the interaction between Au nanoparticles and OVs from the  $SrTiO_3$  [85].

### 3.4. *In Situ DRIFTS*

The formation of surface species after the exposure of the tested (selected) photocatalysts to  $CO_2$ , and the influence of light irradiation on the  $CO_2$  adsorption, were studied using *in situ* DRIFTS. The spectral differences during  $CO_2$  adsorption in the dark *vs.* under irradiation may be caused by: (1) light induced oxygen desorption and implicitly increased amount of Lewis acid sites [86], (2) different activation of adsorbed  $CO_2$ , (3) different interaction of  $CO_2$  with pre-adsorbed hydroxyl groups, (4) enhanced splitting of hydroxyl groups and transfer of hydrogen to adsorbed  $CO_2$  [87].

From the spectra presented in Figures SI-23 – SI-28, it can be concluded, that no considerable differences were observed for all four studied photocatalysts (Au-NiO/STO-SCO (HT), Au-STO-SCO (HT), NiO/STO-SCO (HT) and STO-SCO (HT)) under dark conditions. In other words, the presence of ~0.3 wt:% NiO and ~1 wt:% Au has negligible effect on  $CO_2$  adsorption in the dark. In the studied spectra the observed species were identified to be linearly adsorbed  $CO_2$ , monodentate carbonate, monodentate bicarbonates and carboxylates. In addition to the previously identified species, bidentate carbonate was identified in the spectra of Au-STO-SCO (HT). Under (visible or UV-A) light irradiation though, remarkable differences were identified. One considerable difference is related to the visible-light induced transformation of monodentate bicarbonates over Au-NiO/STO-SCO (HT). Finally, regardless of the thermal treatment performed before  $CO_2$  adsorption (described in the Experimental Section), the vibration feature corresponding to the COH bending (at  $1222\text{ cm}^{-1}$ ) was always observed, which is a clear indication of the presence of hydroxyl groups on the surface for all studied samples.

### 3.5. *Photocatalytic $CO_2$ reduction*

The products formed and their normalized concentrations (in  $\text{ppm g}_{\text{cat}}^{-1} \text{ h}^{-1}$ ) from the photoreduction of  $CO_2$  using  $SrTiO_3$ -based catalysts und Hg-Xe light irradiation are presented in Figure 8. Beyond the presented results, additional samples were analyzed, namely STO-SCO (SM), SCO and Au-SCO. No product formation was observed in the case of SCO and Au-SCO. The activity of STO-SCO (SM) was  $17\text{ ppm} \cdot \text{g}_{\text{cat}}^{-1} \cdot \text{h}^{-1}$  towards  $CH_4$  generation.

Considerably higher activity and selectivity was observed in the case of STO-SCO (HT)-supported *vs.* STO-supported samples. To understand the differences in activity in case of STO- and STO-SCO-based samples, the charge transfer mechanism was studied. Conduction

(CB) and valence band (VB) edges of the single components (SrTiO<sub>3</sub>, SrCO<sub>3</sub>, and NiO) were calculated using experimental results (Mott-Schottky plot, band gaps) and literature reported data. Additionally, the electronic properties of SrTiO<sub>3</sub> and SrCO<sub>3</sub> were calculated using DFT. The main aspects related to the calculations will be presented shortly in the next section.

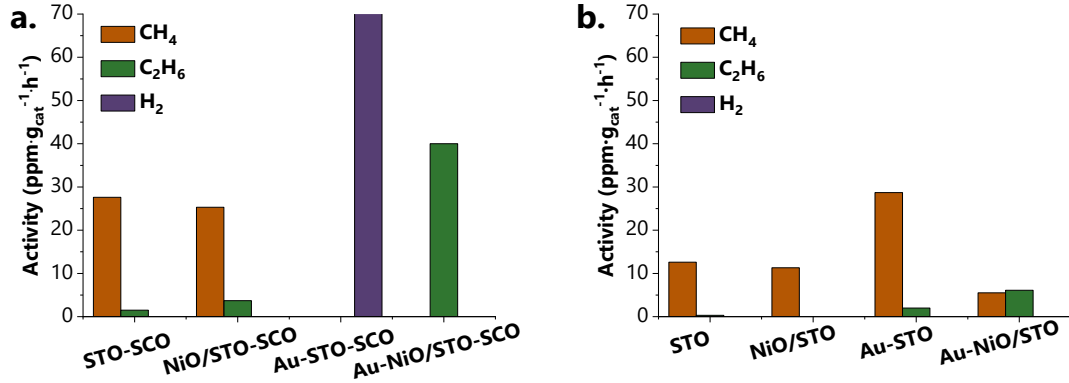


**Figure 8.** The activity of the STO-SCO (HT)-based samples. b. The activity of the reference series of samples (i.e., STO-based samples)

### (1) Influence of SrCO<sub>3</sub>.

(1.1) Several scientific works (Li and coworkers [71], Jin and coworkers [69]) report that the efficient charge separation is given by the functionality of SrCO<sub>3</sub> as an electron trap. This approach assumes the accumulation of electrons in the CB of SrCO<sub>3</sub>, and the localization of holes at the VB of SrTiO<sub>3</sub>. However, based on this charge transfer scheme, it is highly possible that CO<sub>2</sub> reduction would take place over SrCO<sub>3</sub>. At the same time, it must be highlighted that this approach does not account for the band bending and the formation of an electric field. One can explain the validity of this approach by the fact that since SrCO<sub>3</sub> is an insulator, no charge transfer would take place (given by the large work function difference between SrTiO<sub>3</sub> and SrCO<sub>3</sub>), and subsequently, there would be no band bending or generation of an interfacial electric field.

(1.2) With the building of a semiconductor-insulator (SrTiO<sub>3</sub>-SrCO<sub>3</sub>) heterojunction a Fermi level alignment between SrTiO<sub>3</sub> and SrCO<sub>3</sub> might occur resulting in the formation of a built-in electric field which points from SrTiO<sub>3</sub> to SrCO<sub>3</sub> as suggested by Han [88] (Figure 9). Considering the direction of the built-in electric field, the transfer of the electrons from the CB of SrTiO<sub>3</sub> to the CB of SrCO<sub>3</sub> is not possible. However, during the heterojunction formation, generation of OVs and surface doping of SrCO<sub>3</sub> might occur leading to the formation of an intermediate electronic level (IL) over the SrCO<sub>3</sub> part near the interphase for which  $|E_{VB} - E_{IL}| = \Delta E_{(VB-IL)} \leq h\nu$ . At such circumstance, under irradiation a translocation of electrons from the VB of SrCO<sub>3</sub> to its IL and from there to the CB of SrCO<sub>3</sub> would be possible. Electrons from the IL of SrCO<sub>3</sub> might be also transferred to the VB of SrTiO<sub>3</sub>, where they can recombine with holes from VB of SrTiO<sub>3</sub> which will suppress charge carrier recombination between  $h_{VB,SrTiO_3}^+$  and  $e_{CB,SrTiO_3}^-$ .

To investigate the possibility of a built-in electric field formation in case of SrTiO<sub>3</sub>-SrCO<sub>3</sub> the work function (and implicitly the Fermi level) of the pure (i.e., SrTiO<sub>3</sub>, SrCO<sub>3</sub>) and doped materials (C-doped SrTiO<sub>3</sub>, Ti-doped SrCO<sub>3</sub>) was calculated *via* computational methods.

The SrTiO<sub>3</sub>(110) and SrCO<sub>3</sub>(111) slab models were built. As to SrTiO<sub>3</sub>(110), two different terminations (SrO- and TiO-) were considered. To study the interaction between SrTiO<sub>3</sub>(110) and SrCO<sub>3</sub>(111), both terminations of SrTiO<sub>3</sub>(110) were doped by a C atom, i.e., one surface Ti atom was replaced by a C atom. As to SrCO<sub>3</sub>(111), one surface C atom was replaced by a Ti atom.

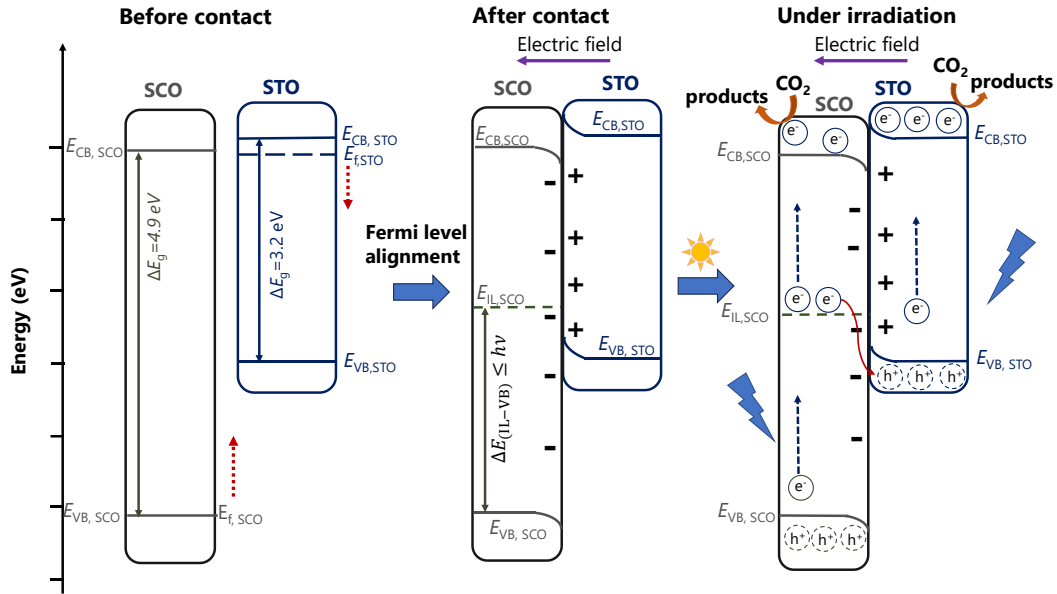


**Figure 9.** Scheme of charge transfer in case of SrTiO<sub>3</sub>-SrCO<sub>3</sub> *via* accounting the formation of internal electric field – rebuilt based on the work written by Han and coworkers [88] (CB – conduction band, IL – intermediate level, SCO – SrCO<sub>3</sub>, STO – SrTiO<sub>3</sub>, VB – valence band; Remark: The red arrows in the left side ("before contact") indicate the Fermi level alignment of each component).

Then, the density of states of all the surfaces was calculated. Furthermore, the work function ( $\Phi$ ) was calculated based on  $\Phi = E_{vac} - E_f$  ( $E_{vac}$  is vacuum potential and  $E_f$  is the Fermi energy). The work functions are listed in Table 3. Based on the computational results listed in Table 3, the termination of SrTiO<sub>3</sub> (either SrO- or TiO-terminated, cases 1.1 and 1.2) influences significantly the absolute value of the work function (i.e., 5.7 vs. 2.1 eV). The computational results support the hypotheses related to the direction of Fermi level shift (Table 3,  $\Delta\Phi$ ) after the interaction between the two components (as marked in Figure 9).

**Table 3.** Calculated work function of different surfaces

Case	Surface	$\Phi$ (eV)	Modified surface	$\Phi$ (eV)	$\Delta\Phi$ (eV)
1. SrTiO <sub>3</sub>	1.1. SrO-terminated SrTiO <sub>3</sub> (110)	5.7	C-doped SrO-terminated SrTiO <sub>3</sub> (110)	6.1	0.4
	1.2. TiO-terminated SrTiO <sub>3</sub> (110)	2.1	C-doped TiO-terminated SrTiO <sub>3</sub> (110)	2.3	0.2
2. SrCO <sub>3</sub>	SrCO <sub>3</sub> (111)	5.7	Ti-doped SrCO <sub>3</sub> (111)	5.3	-0.4

Methane formation rate during batch cleaning (gas mixture: He+H<sub>2</sub>O) over STO-SCO (HT) catalysts was higher when compared to that of STO (which indicates the participation of SrCO<sub>3</sub> on CH<sub>4</sub> formation. Here, the CH<sub>4</sub> might be formed by the reaction of adsorbed carbon species under photogenerated charge carriers. Because no methane formation was observed when using SCO, it is assumed that the higher activity of STO-SCO (HT) compared to STO is mainly caused by a larger number of photocatalytic active species. However, the direct participation of the SrCO<sub>3</sub> phase on product formation over STO-SCO (HT) cannot be excluded completely. To exclude the influence of the structural peculiarities of SrCO<sub>3</sub> and SrTiO<sub>3</sub> when it comes to the hydrothermally synthesized and commercially available samples (different morphology), the activity of STO and of STO-SCO (SM) in CO<sub>2</sub> reduction (or batch cleaning) were also compared (i.e., 12 vs. 17 ppm·g<sub>cat</sub><sup>-1</sup>·h<sup>-1</sup> STO vs. STO-SCO (SM)). Again, the presence of SCO (in STO-SCO (SM)) leads to higher activity.

(2) Influence of NiO. The charge transfer mechanism (mainly for photocatalytic H<sub>2</sub>O splitting) has already been reported for NiO/SrTiO<sub>3</sub> [68, 89] and NiO/TiO<sub>2</sub> [78, 79].

The functionality of NiO remains the same in case of NiO/STO-SCO (HT) systems (considering the alignment of Fermi levels) as long as  $\Phi(\text{STO-SCO(HT)}) < \Phi(\text{NiO})$ . However, because of the low NiO content in the composite, the overall effect of NiO on CO<sub>2</sub> reduction was expected to be relatively low (Figure 8: STO vs. NiO/STO, STO-SCO (HT) vs. NiO/STO-SCO (HT)).

(3) Influence of Au. Analyzing the hypothetical charge transfer mechanism in Au-SrTiO<sub>3</sub> [90], electrons are injected from Au to the CB of SrTiO<sub>3</sub>, and CO<sub>2</sub> reduction occurs over SrTiO<sub>3</sub>. However, if SrCO<sub>3</sub> is present, and the Fermi level alignment between SrTiO<sub>3</sub> and SrCO<sub>3</sub> takes place prior contact with Au. According to the aligned Fermi level between SrTiO<sub>3</sub> and SrCO<sub>3</sub>, different mechanisms are probable. If  $E_{F, \text{aligned}}(\text{SrTiO}_3\text{-SrCO}_3) < E_F(\text{Au})$ , the internal electric field will point from the metal (Au) to SrTiO<sub>3</sub>-SrCO<sub>3</sub>, which guides the electrons from the support to Au [90]. In the contrary case ( $E_{F, \text{aligned}}(\text{SrTiO}_3\text{-SrCO}_3) > E_F(\text{Au})$ ), a charge carrier transport similar to Au-SrTiO<sub>3</sub> occurs.

Enhanced CH<sub>4</sub> production was observed over Au-STO vs. STO samples (Figure 7.b), which can be correlated with the involvement of Au NPs as an electron donor. In contrast to this, over Au-STO-SCO (HT) the formation of carbon-based products in presence of CO<sub>2</sub> was similar as for batch cleaning and H<sub>2</sub> was the main product in CO<sub>2</sub> reduction over this catalyst. One reason for the various reaction products obtained over Au-STO and Au-STO-SCO (HT) might be the differences between the Fermi level of the corresponding support and the Fermi level of Au.

(4) Mutual effect of Au and NiO in STO-based systems.

STEM and SEM results give no hints of Au-Ni alloy formation. According to Figure 8, CO<sub>2</sub> reduction over Au-NiO/STO takes place with lower rates as in the case of Au-STO (Figure 8.b). Interestingly, already the presence of both NiO and Au on STO alone improves C<sub>2</sub>H<sub>6</sub> formation slightly compared to the pure support. However, over Au-NiO/STO-SCO (HT) (Figure 8.a) C<sub>2</sub>H<sub>6</sub> was observed as the single product with relatively high formation rate. Formation of C<sub>2</sub> products from CO<sub>2</sub> followed a complex reaction pathway whose key step is a C-C coupling [91]. It seems that the simultaneous presence of Au and NiO supports such coupling processes

which occur in monometallic catalysts only in minor extent. The role of the single compound in the C<sub>2</sub> formation process is still unclear. One reason for the high C<sub>2</sub>H<sub>6</sub> selectivity might be an increased local temperature of the Au-NiO/STO-SCO (HT) surface (given by the simultaneous presence of a Schottky junction and OVs, as suggested by Cai and coworkers [80]) which facilitates the mobility of the intermediates formed as well as the desorption of the C<sub>2</sub> products from the surface of the photocatalyst [80]. Thereby, the NiO might play a role in the activation of CO<sub>2</sub> [87].

#### 4. Conclusions

In summary, the individual and simultaneous influence of SrCO<sub>3</sub>, NiO and Au on the photocatalytic CO<sub>2</sub> reduction activity of SrTiO<sub>3</sub>-based materials was studied. Based on experimental and computational investigations the following conclusions can be drawn:

**The presence of SrCO<sub>3</sub>** has a positive effect on the photocatalytic activity of SrTiO<sub>3</sub> in CO<sub>2</sub> reduction. It is assumed that by using a SrTiO<sub>3</sub>-SrCO<sub>3</sub> heterojunction a higher number of reactive species are available for the reaction under irradiation compared to pure SrTiO<sub>3</sub>.

**The low amount of NiO (0.3 wt%)** (on either supports: SrTiO<sub>3</sub>, SrTiO<sub>3</sub>-SrCO<sub>3</sub>) has only a minor effect on the activity and product formation.

CO<sub>2</sub> reduction products of **Au containing samples** are affected by the support. In case of Au-SrTiO<sub>3</sub> mainly CH<sub>4</sub> was formed, whereas for Au-SrTiO<sub>3</sub>-SrCO<sub>3</sub> H<sub>2</sub> was the main product. This difference in product formation might be explained by considering Fermi level alignment.

**The simultaneous presence of Au and NiO** on SrTiO<sub>3</sub>-SrCO<sub>3</sub> surface supports the dimerization of C<sub>1</sub> intermediates.

## (2.4) Experimental and numerical investigations of flow behavior in an open falling film microreactor equipped with curved flow splitting elements\*\*

### 1. Introduction

Falling film microreactor (FFMR) is a well-known representative of continuous-phase microstructured systems [92], where the liquid film flow is gravity-driven [92]. Different reactor designs were implemented for G-L contacting, such as spherical, cylindrical and flat [93]. The reported range of film thickness is situated between 0.5-3.0mm in conventional falling film systems [32, 94], however generation of stable films with thickness up to 100  $\mu\text{m}$  was reported in the case of FFMR developed by IMM (Institut für Mikrotechnik Mainz) [32].

Recently, considerable interest has been provided towards the conduction of photo-driven reactions in FFMR equipped with an inspection window (e.g., dye-sensitized transformation of 1,5 dihydroxynaphthalene [30], photo-oxidation of  $\alpha$ -terpinene [95]), offering promising light penetration properties.

Extensive CFD studies were conducted in order to obtain a better understanding on the G-L flow in FFMR, however in most of the cases only single phase was simulated (e.g., gas phase [31, 96]). The scientific work published by Ho and coworkers can be considered as a milestone in the numerical investigation of the G-L flow in FFMR, since both phases were considered during the modeling.

This work aims to provide an experimental insight into the liquid phase flow of the reactor including curved flow-splitting elements at the distributor part and 64 channels as well as the G-L flow situation in open microchannels. The experimental assessment of the flow situation is carried out *via* pulse tracer experiment, holdup measurements, in combination with CFD study.

### 2. Material and methods

*Experimental setup.* According to Figure 10.a, the main constitutive elements of the studied Falling Film Microreactor (FFMR, Little Things Factory, Elsoff, Germany, Figure 10.a-c) are: (i) upper cover plate, also called as top reactor module containing an open rectangle (e.g. for using a translucent window, length: 66 mm, width: 80 mm, radius=3.5 mm), (ii) removable structured reaction plate and (iii) fixed heat exchanger module. The reaction plate is placed between the fixed heat exchanger module and the upper cover plate, as shown in Figure 10.a-c. The inlets and outlets for the gas (marked with green) and liquid (inlet: blue, outlet: red) phases are positioned on the top housing module (as marked in Figure 10.a). However, it should be emphasized that no gas flowed into the reactor during the experiments. As the rectangular opening on the upper housing module was not closed during the study, open channel conditions were ensured for all 58 visible channels along a certain channel length (66 mm). The opening allows not only the direct observation of the liquid flow distribution [31], but also the usage of this reactor for photocatalytic applications. A specific split and curve structure, 64

---

\*\* Bîborka Boga, Kevin Baur, Vasile-Mircea Cristea, Norbert Steinfeldt, Norbert Kockmann, Experimental and numerical investigations of flow behavior in an open falling film microreactor equipped with curved flow splitting elements *Chemical Engineering Science*, 2024, 298, 120338 (DOI: 10.1016/j.ces.2024.120338)

microchannels (with a total length of 100 mm, width of 0.9 mm and the depth of 0.5 mm) and a collector domain are embedded in the reaction plate (Figure 10.b). Unidirectional network with fork-like structure is characteristic for the distribution part [97], as depicted in Figure 10.b.

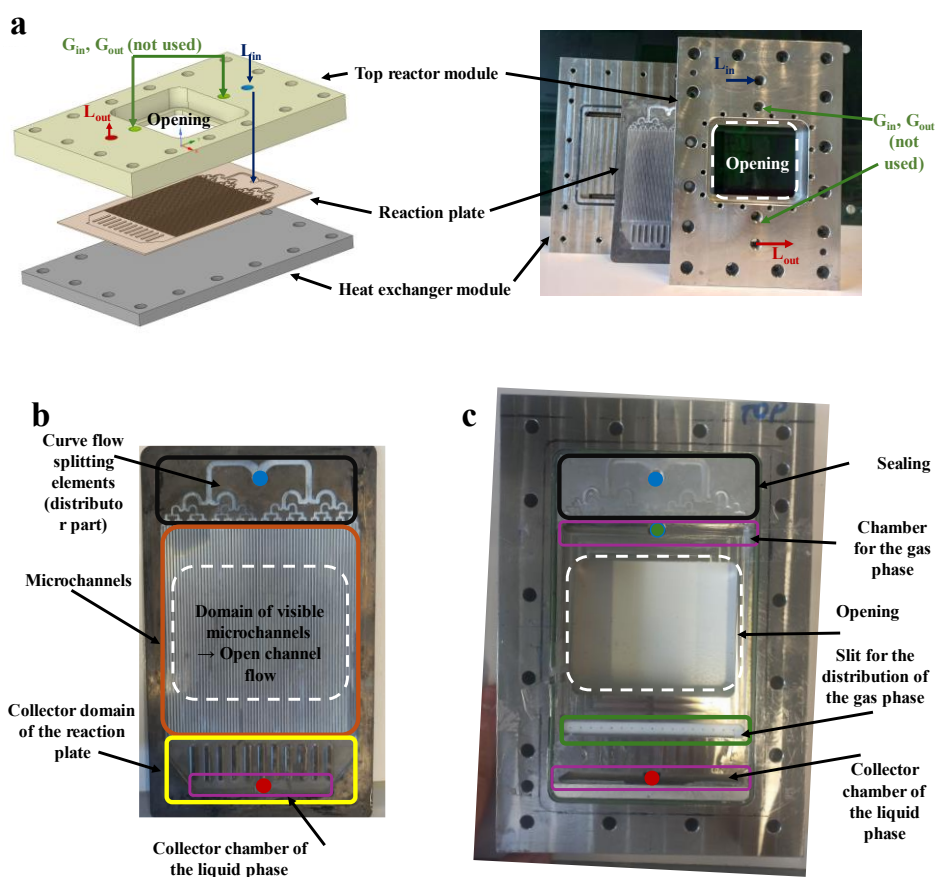


**Figure 10.** a. Exploded view of FFMR, b. Reaction plate, c. Back side of the top cover reactor module.

The desired flowrate at the inlet of FFMR was assigned by a high precision HPLC pump (PrepStar, Varian, USA). The liquid was sucked out from the collector part (Figure 10.c) by a peristaltic pump (type FF201-60, Cole-Parmer Instrument, USA). The inclination angle between the FFMR and the horizontal plane was fixed *via* a support with an angle of  $35^\circ$ .

#### *Experimental characterization of the flow situation in FFMR*

*Pulse input tracer experiments.* By assuring different inlet flow rates (i.e.,  $2\text{-}14\text{ mL}\cdot\text{min}^{-1}$ ) for the selected studied liquids (water and ethanol), the injection of the fluorescent tracer was performed by a six-port valve (VICI Valco Instruments Co Inco, Model E60, Serial 39611,  $V_{loop}=150\ \mu\text{L}$ ), which was inserted between the HPLC pump and the reactor inlet. The visualization of the fluorescent tracer was carried out by using a UV lamp (KW 254 nm, LV 366 nm) and digital camera. The extraction of frames from equidistant timeframes was performed *via* Openshot software. The processing of the extracted frames included (i) delimiting and nomenclating the channels, (ii) measuring the distance from the front until the tracer pathway, (iii) estimation of the maximum velocity and residence time.

*Liquid holdup measurements.* Liquid holdup in the studied FFMR was calculated as the fraction (volume) of the split & curve structure, microchannels and collector part of the reactor occupied by the liquid phase.

*Capillary forces in the microchannels.* The self-developed method is based on placing both coated and uncoated reactor plates in a vertical position in a reservoir filled with water or ethanol. To quantify the capillary effect, the height of the rise of the liquid in the microchannels was determined.

*Contact angle.* A specialized microscope (Leica Z16 APO, Switzerland) was used for the visualization of the static contact angle by applying a droplet on the studied surfaces (stainless steel and coated surface).

#### *Coating of the reaction plate, and its characterization*

Optimized suspension deposition method was applied for the deposition of commercial titania (P25, Merck, Germany) in the split & curve structure and in the microchannels. The coating at the bottom and sidewalls was assessed *via* the previously described specialized Leica Microscope.

#### *Empirical assessment of the flow behavior*

The information obtained from the empirical correlations have been used to roughly estimate the flow characteristics (i.e., flow regime) for the implementation of the 2D and 3D simulations in ANSYS Fluent. Detailed discussion about the empirical correlations can be found in the main text of the manuscript.

#### *Simulation of the multiphase flow*

First, transient 2D multiphase simulations were implemented to obtain an overview on the physics of the flow in the microchannel in ANSYS Fluent 2023 R1, followed by the implementation of the 3D simulations (with similar specifications) for a representative domain of the microchannel.

*Geometry.* The geometry used for the 2D, and 3D simulations was constructed in Space Claim (Ansys 2023 R1).

*Meshing.* The grid generation was performed using ANSYS Meshing 2023 R1, which was further imported into Fluent. "Hexa" elements were used as control volumes for the generation of the computational grid.

*Setup.* The Volume of Fluid (VoF) multiphase model was applied, which is an interface-tracking method used for the simulation of free surfaces.

### **3. Results and discussions**

#### *3.1. Experimental results*

*Pulse input tracer experiments* were performed to assess the flow distribution in the microchannels (and implicitly to determine the range of flowrates which leads to relatively uniform flow distribution), and to estimate the maximum velocity and the hydraulic residence time in the microchannels.

*Stainless steel - Ethanol.* The studied inlet assigned flowrates were 2, 4, 8, 12, 14 mL·min<sup>-1</sup>. While relatively uniform distribution was observed in the case of flowrates 4, 8, 12 mL·min<sup>-1</sup>, overflow was identified when 14 mL·min<sup>-1</sup> was assigned at the inlet. Already when the assigned flowrate was 12 mL·min<sup>-1</sup>, the cross-contamination of certain channels can be observed, which may be correlated with the capillary effects.

*Stainless steel - Water.* The tracer experiments with water were performed in a similar manner as in the previous case (i.e., Stainless steel – Ethanol), however at this time the UV assisted detection of the tracer was not possible in the microchannels. To increase the visibility of flow situation in the microchannels, the irradiation and recording conditions were modified. To further evaluate the poor wetting ability of the stainless steel by water, the contact angle ( $\theta$ ) was experimentally assessed. Relatively high contact angle was observed at the steel-water-air interface, which provided explanation for the poor wettability.

*Coated microchannels - Water.* Since many gas/liquid reactions can be performed in aqueous solution, the surface hydrophilicity of the steel reaction plate was increased by titania deposition with the aid of an airbrush using commercially available TiO<sub>2</sub> (P25) as coating layer. The plate was weighted before and after deposition. Assuming that titania was deposited only on the channel ground, a maximum layer thickness of 0.36  $\mu\text{m}$  was estimated. Otherwise, although all the channels were wetted, no uniform flow distribution could be obtained using a flow rate of 4 mL·min<sup>-1</sup>. The overflow in certain channels could be observed when flow rate of 12 mL·min<sup>-1</sup> was applied. Therefore, results of tracer experiments with flow rates of 6, 8 and 10 mL·min<sup>-1</sup> were depicted for the coated-microchannels – water -air system (Figure 11.a-c). The estimated average velocity values were 16, 22 and 22.5 mm·s<sup>-1</sup> for the previously mentioned selected flow rates (i.e., 6, 8, 10 mL·min<sup>-1</sup>).

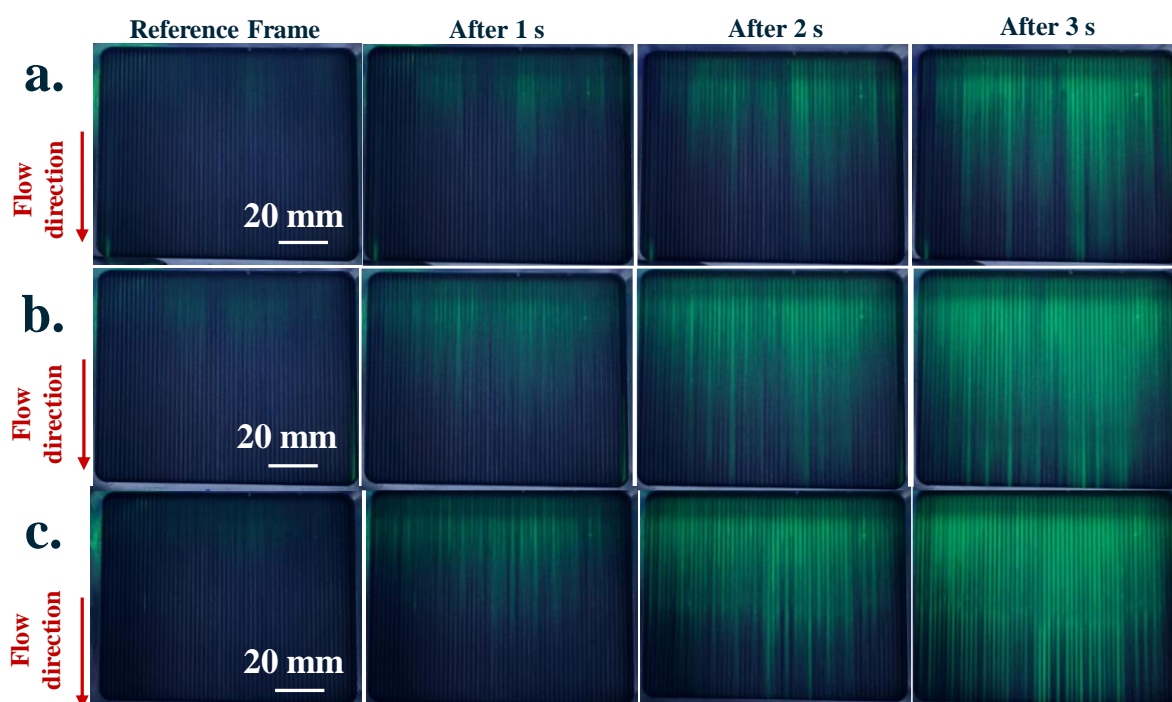


**Figure 11.** Extracted frames showing the temporal evolution of fluorescein in the case of coated microchannels – water – air system when the assigned flow rate of the liquid phase was a. 6, b. 8 or c. 10 mL·min<sup>-1</sup>

While the estimated mean residence time was  $\sim 5.83$  s when  $6 \text{ mL}\cdot\text{min}^{-1}$  was assigned as global inlet flow rate, this characteristic time decreased to 4.88 and 4.23 s for 8 and  $10 \text{ mL}\cdot\text{min}^{-1}$ , respectively. The estimations of residence time of the liquid phase in single channels for stainless steel-ethanol-air system were carried out as given in Table 4.

**Table 4.** Theoretical and experimental mean values of the hydraulic residence times ( $\langle\tau_{\text{theo}}\rangle$  and  $\langle\tau_{\text{exp}}\rangle$ )

$Q_{\text{global}}$ ( $\text{mL}\cdot\text{min}^{-1}$ )	Coating layer - water			Stainless steel-ethanol		
	$\langle\tau_{\text{theo}}\rangle$ (s)	$\langle\tau_{\text{exp}}\rangle$ (s)	$SD$ (s)	$\langle\tau_{\text{theo}}\rangle$ (s)	$\langle\tau_{\text{exp}}\rangle$ (s)	$SD$ (s)
4	4.15	--	---	4.72	7.00	3.24
6	3.17	5.83	2.49	3.60	--	--
8	2.16	4.88	2.01	2.98	6.92	3.70
10	2.25	4.24	1.82	2.56	--	--
12	2.00	--	--	2.27	3.96	1.93

Table 4 compares values from the experimental determined hydraulic residence time ( $\langle\tau_{\text{exp}}\rangle$ ) with the theoretically calculated values ( $\langle\tau_{\text{theo}}\rangle$ ). The estimated experimental residence time ( $\langle\tau_{\text{exp}}\rangle$ ) values were higher in comparison to the empirically calculated ones ( $\langle\tau_{\text{theo}}\rangle$ ), which was considered as an indication about the development of thicker liquid film in the microchannels as expected from the Nusselt theory. The calculated standard deviation (SD) of the experimental residence time values in provides indication about the uniformity of the residence time (and velocity) in the 58 (visible) microchannels of the studied reactor. In other words, as the SD was lower, as the uniformity of residence time distribution (and velocity) was improved. In general, SD decreased with increasing flow rate. Relatively uniform residence time distribution was observed in the case of coating layer-water-air *vs.* stainless steel-ethanol-air system (Table 4).

To obtain further insight about the film thickness and residence time, liquid holdup measurement with an inlet flowrate of  $8 \text{ mL}\cdot\text{min}^{-1}$  was performed in recirculation mode. Considering that the collector part is fully filled with water, the ratio between the occupied volume *vs.* maximum volume is 0.92, which again indicates that the real liquid film thickness values are higher than the empirically calculated ones.

Furthermore, based on the self-designed experiments aiming the assessment of the capillary forces it can be concluded that the manifestation of the capillary forces in the  $\text{TiO}_2$ -coated microchannels was the most considerable using water as liquid phase.

### 3.2. Empirical assessment of the flow situation

Since  $Re_L < 20$ , this indicates that laminar flow with negligible rippling is characteristic for the studied system [98]. Furthermore, Bond (Bo), capillary (Ca) and Weber (We) dimensionless numbers were calculated. In case of microdevices, the typical order of the Bond number is  $10^{-3}$  [99], which is in concordance with our results (Bo: from  $4.53 \cdot 10^{-4}$  to  $1.50 \cdot 10^{-3}$ ). This result confirms the dominance of surface tension force over the gravitational force and is also a clear indication about the manifestation of capillary forces in the microchannel. Moreover, the typical value of the Ca number in case of microdevices is  $10^{-4}$  [99], which is

in agreement with our results. Finally, the surface tension forces have much greater impact on the flow than the inertial forces ( $We < 1$ ) [100]. The empirical results provided not only a basis for comparison for the numerical results (i.e., film thickness and velocity, Figure 12), but also, they assured the correct setup of the simulation (regime, accounting the surface tension effect, etc.).

### 3.3. Simulation of the multiphase flow

As a first approach, 2D simulation of the G-L flow were implemented for selected flowrates (i.e., 2, 4, 6, 8, 10, 12, 14  $\text{mL}\cdot\text{min}^{-1}$ ) according to the specifications described in the Methods section. As it was expected, the results of 2D simulation agree with the empirical results.

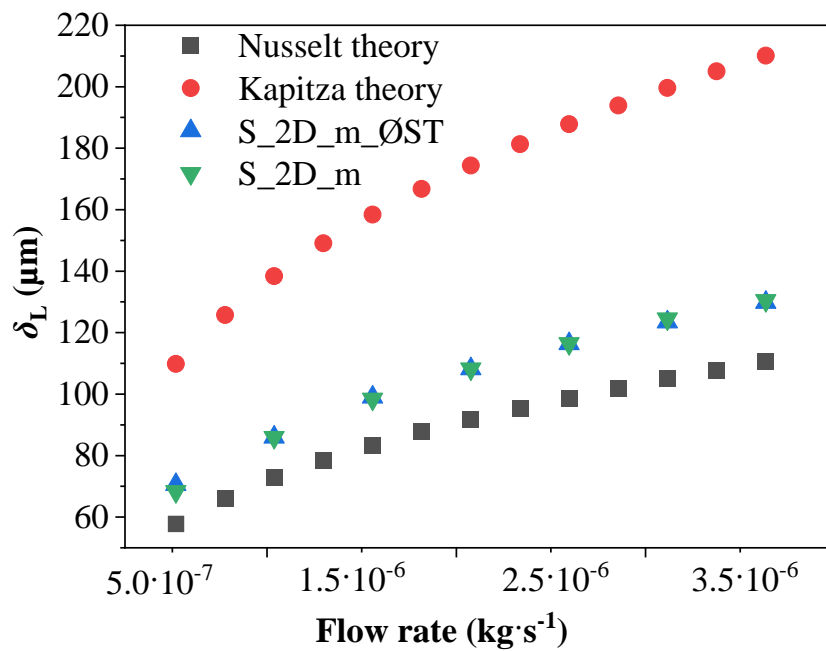


**Figure 12.** Comparison of the numerically (time-averaged values: 0.60-0.80 s for S\_2D\_m\_ØST, and 0.70-0.82 s for S\_2D\_m, at  $x/L_{\text{modelled}} = 0.5$ ) and empirically calculated film thickness values vs. inlet mass flow rate

The importance of 3D simulations is undoubtful given by the competing effect of the sidewalls discussed in detail by Kögel and Aksel, namely: (i) decreased velocity in the vicinity of the walls provided by the nonslip boundary condition, (ii) increased velocity of the fluid in the neighborhood of the walls due to capillary elevation [101]. 3D simulations were implemented assigning as inlet flow rates corresponding to the studied range (i.e.,  $Q_{\text{global}} = 2 - 14 \text{ mL}\cdot\text{min}^{-1}$ ). In contrast to the 2D simulations, the initialization was done with fully filled channel. The steady state conditions were evaluated by analyzing the transient liquid film height at different locations (i.e., at  $x/L_{\text{modelled}} = 0.1, 0.2, 0.3, 0.4, 0.7$ ). The steady state conditions were achieved after 0.17 s in case of all extracted data. To have an overview on the liquid film thickness at different length positions, the liquid film thickness values were averaged in the range of 0.17-0.25 s (at  $y = 0 \text{ mm}$ ), as depicted in Figure 13 (for selected simulations, namely S\_3D\_3, S\_3D\_4, S\_3D\_5). Analyzing Figure 13, one can conclude that the position along the channel length has bigger influence on the film thickness than the actual flowrate assigned in

the simulations. The nonuniformity of the film thickness along the channel length (Figure 13,  $\delta_L(x/L_{\text{modelled}} = 0.1) < \delta_L(x/L_{\text{modelled}} = 0.2) < \delta_L(x/L_{\text{modelled}} = 0.3) < \delta_L(x/L_{\text{modelled}} = 0.4)$ ) may be related to the capillary pressure, and implicitly to the backflow.

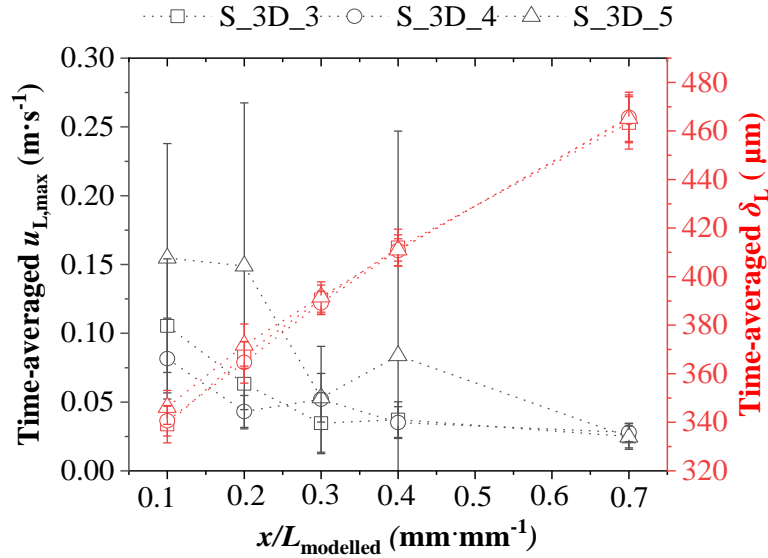


**Figure 13.** Time-averaged film thickness and time-averaged maximum velocity (0.17-0.25 s) from the middle plane (i.e.,  $y = 0$  mm) along the channel length for different flow rates (S\_3D\_3:  $6 \text{ mL}\cdot\text{min}^{-1}$ , S\_3D\_4:  $8 \text{ mL}\cdot\text{min}^{-1}$  and S\_3D\_5:  $10 \text{ mL}\cdot\text{min}^{-1}$ ).

As it was expected, the formation of thicker liquid films was observed in case of 3D simulations (vs. 2D simulation, and the one calculated from empirical correlations), which was also reported by Anastasiou and coworkers in narrow microchannels [102]. The relatively high film thickness (which results a high occupancy of the channels) is in concordance with the film thickness estimated from the liquid holdup measurements (i.e., 92% filling of the channels).

Furthermore, the time-averaged maximum velocity values in the x-direction were analyzed along the channel length as given in Figure 13. The decrease of maximum velocity in the x-direction along the channel length was observed (Figure 13), which is probably given by the backflow phenomena.

To assess the influence of plate inclination angle, simulations with plate inclination angles of  $15^\circ$ ,  $35^\circ$  and  $75^\circ$  were performed and analyzed. As it was expected from the Nusselt theory, higher liquid film thickness value was observed when the plate inclination angle was lower (i.e.,  $15^\circ$  vs.  $35^\circ$ , Figure 14.a). The formation of instable liquid film was observed when the plate inclination angle was set to  $75^\circ$  (Figure 14.a). At high inclination angles (such as  $75^\circ$ ), instabilities caused by the gravitational acceleration *via* the  $g \cdot \sin\beta$  component might occur [103, 104].

To study the effect of GSL contact angle within the wall BC beyond the base case (i.e.,  $\theta = 40^\circ$ , G\_3D\_3), additional simulations were performed by assigning  $10^\circ$  (S\_3D\_3\_con10) and  $70^\circ$  (S\_3D\_3\_con70) as the value of this parameter (i.e., GLS contact angle at the sidewall-water-air interface). Figure 14.b compares the film thickness along the channel width for an identical flow rate and different contact angles. The results can be only explained by differences

in the flow velocity (i.e., higher velocity in case of thinner liquid film thickness, i.e., higher contact angle).

The differences of interface curvature length were minor when the assigned contact angle was  $10^\circ$  or  $40^\circ$ . In contrast to this, considerably lower length of interface curve was identified when the contact angle was  $70^\circ$ .

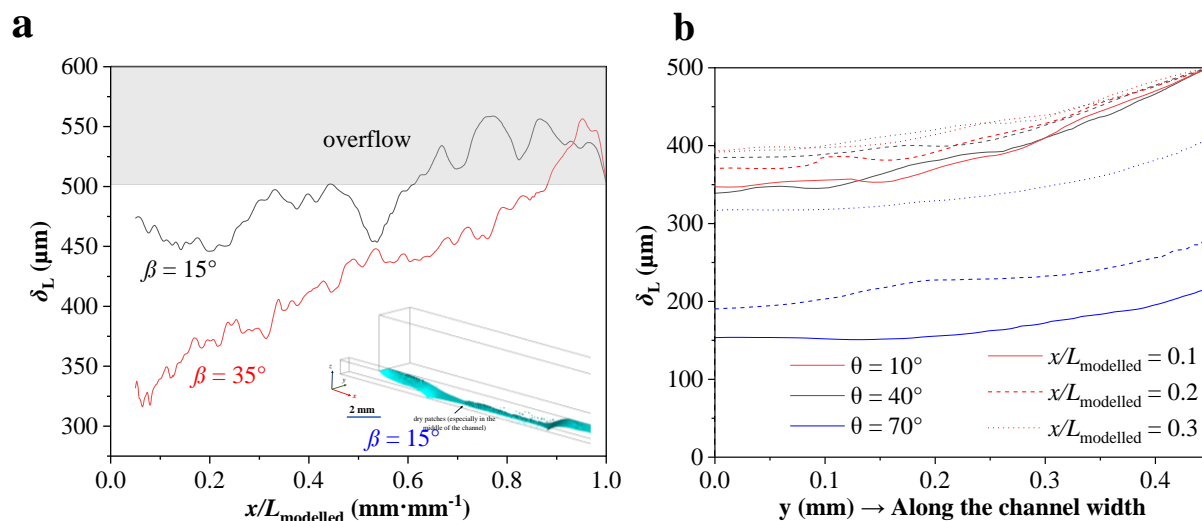


**Figure 14.** a. The liquid film thickness along the channel length at  $y = 0$  mm with different plate inclination angles at  $t = 0.25$  s. b. The free surface profile (YZ plane) when  $\theta = 10^\circ$ ,  $40^\circ$  or  $70^\circ$  after achieving the steady state conditions (global flow rate  $6 \text{ mL}\cdot\text{min}^{-1}$ ).

#### 4. Conclusions

This work was aiming the characterization of a falling film microreactor with curved flow splitting elements and 64 microchannels. This study offered an insight into the G-L (i.e., air-water, air-ethanol) flow situation in the open microchannels (uncoated – stainless steel and titania-coated) *via* experimental and numerical methods. Similar operating flow rate regimes ( $4 - 12 \text{ mL}\cdot\text{min}^{-1}$ ) were determined for the stainless steel – ethanol and titania-coated channels – water system. The higher experimental residence time values (*vs.* empirical values) indicated the formation of higher liquid film thickness as the one calculated from Nusselt and Kapitza theory. It was demonstrated that the titania coating has led to the decrease of GLS contact angle at coated layer-water air interface (improved wettability), and to the reinforcement of capillary pressure *via* the pores in the catalyst structure. Especially this latter causes the formation of higher interfacial area (between the liquid film and gas phase), which can contribute to an enhancement of the G-L mass transfer. Both the experimental assessment (liquid holdup measurement) and simulation results confirmed the formation of thicker liquid film thicknesses as expected from Nusselt theory which is important to know when using the reactor for chemical reactions. A backflow is assumed as the reason for the higher film thickness.

Considering the results from the 3D simulations, beside the already known parameters like channel geometry and liquid surface tension, the flow behavior inside a single channel is also strongly affected by the wall adhesion (at the sidewalls) and the GLS contact angle. The latter can be controlled by the deposited solid material. Furthermore, the simulations show that the

flow pattern inside the channel depends on the inclination angle of the reaction plate. At too small inclination angle an overflow can occur already before the end of the channel and at too high inclination angles destabilization of the liquid film can appear. These findings provide important contribution for the design of falling film microreactor with immobilized catalyst layer.

## **(2.5) Photocatalytic antibiotic degradation in coated open microchannels by applying 2D and 3D flow modeling with kinetics<sup>††</sup>**

One of the centerpieces of European Environmental Policy is to ensure that every citizen is granted access to clean water. Growing health problems have been associated with the presence of active pharmaceutical ingredients in drinking water in case of European and Asian nations at relatively high concentrations [105].

In this work, the photocatalytic degradation of ciprofloxacin, a well-known representative of fluoroquinolone antibiotics [106], has been studied in a falling film microreactor prototype (fabricated by Little Things Factory, Elsoff, Germany) with 64 open microchannels. The microchannels were coated with a thin TiO<sub>2</sub> (P25) layer *via* slurry washcoating method. For the modeling of the studied photoreactor the coupled mass and momentum conservation law was considered given by the operation regime of the photoreactor. The Langmuir-Hinshelwood model was used for the description of the kinetics of the degradation of ciprofloxacin in the previously mentioned reactor. The characteristic parameters from the Langmuir-Hinshelwood model, namely the adsorption constant and the Langmuir-Hinshelwood rate constant, were fitted with the consideration of the 2D and 3D models of the photoreactor. The investigations highlighted the importance of 3D models in case of microreactors given by the considerable influence of the sidewalls on the flow characteristics and on mass transfer of components.

*Remark: This research work is in progress of publication.*

---

<sup>††</sup> Biborka Boga, Kevin Baur, Elisabeta-Cristina Timiș, Henrik Lund, Tim Peppel, Vasile-Mircea Cristea, Norbert Kockmann, Norbert Steinfeldt, Photocatalytic antibiotic degradation in coated open microchannels by applying 2D and 3D flow modeling with kinetics, *Journal of Environmental Chemical Engineering*, Submission in progress

### Chapter 3. Final conclusions

**Section 2.1** is focused on the optimization of photocatalytic activity of CaTiO<sub>3</sub> for rhodamine B degradation in a slurry-type annular photoreactor with external irradiation. The synthesis design of CaTiO<sub>3</sub> was performed according to the Box Behnken design considering the synthesis temperature, duration, concentration of shaping agent and the type of Ca<sup>2+</sup> precursor as input parameters. 30 designed catalysts were prepared *via* hydrothermal crystallization, followed by their photocatalytic assessment. The conversion of rhodamine after 4 hours under the studied experimental conditions was between 22-80%. Different empirical models, namely second-order polynomial regression, and artificial neural network models, were implemented to describe the relationship between the synthesis conditions and photocatalytic efficiency. The implemented models were used for optimization. The optimization resulted to an enhancement of the photocatalytic activity to 96% under the studied conditions.

#### Personal contributions:

- Identification of the key parameters/descriptors (i.e., synthesis temperature and duration, concentration of the shaping agent, as well as the type of Ca<sup>2+</sup> precursor), which have considerable influence on the structural properties of the catalyst, and implicitly on photocatalytic performance.
- Finding the optimum synthesis conditions of CaTiO<sub>3</sub>, which lead almost to maximum conversion of rhodamine B under the studied conditions (~96%)
- Integration of mathematical modelling into materials science for the optimization of the catalyst.

In **section 2.2**, different strategies aimed at the control of SrCO<sub>3</sub> content of SrTiO<sub>3</sub>-SrCO<sub>3</sub> heterojunctions are presented. The first strategy was based on (i) reducing the K<sub>2</sub>CO<sub>3</sub> content of KOH (*via* purification method with CaO described in the literature), and (ii) lowering the possibility the dissolution of airborne CO<sub>2</sub> into the reaction mixture (*via* conduction of the homogenisation step under Schlenk line). The SrCO<sub>3</sub> content of the SrTiO<sub>3</sub>-SrCO<sub>3</sub> catalyst was diminished to 5 wt%. Another strategy was the addition of an excess from the Sr<sup>2+</sup> precursor (Sr<sup>2+</sup>: Ti<sup>4+</sup> = 1:1 or 1.25:1), which facilitated the simultaneous formation of SrCO<sub>3</sub> (21 *vs.* 15 wt% SrCO<sub>3</sub>) during the hydrothermal synthesis of SrTiO<sub>3</sub>. Finally, the last strategy was based on the application of different Ti<sup>4+</sup> precursors (pure anatase *vs.* P25), which led to a content of 15 wt% SrCO<sub>3</sub> (when the Ti<sup>4+</sup> precursor was pure anatase) and 24 wt% SrCO<sub>3</sub> (when the Ti<sup>4+</sup> precursor was P25) in the final catalyst. The presence of SrCO<sub>3</sub> was beneficial and resulted in an enhanced photocatalytic efficiency for both oxidation and reduction processes. 21 wt% was the optimum SrCO<sub>3</sub> content which resulted in the highest mineralization of diclofenac in aqueous solution (62%) under the studied conditions. The terephthalic acid hydroxylation experiments (photoluminescence) confirmed the generation of 3.5 times higher amount of hydroxyl radical in the presence of SrTiO<sub>3</sub>-SrCO<sub>3</sub> *vs.* SrTiO<sub>3</sub>. Beyond the relatively high concentration of hydroxyl radical, the carbonate anion radical might contribute to the enhancement mineralization of diclofenac under the studied conditions.

### Personal contributions:

- Identification of the synthesis parameters which have direct influence on the SrCO<sub>3</sub> content of the SrTiO<sub>3</sub>-SrCO<sub>3</sub> heterojunction synthesized *via* hydrothermal crystallization, namely the K<sub>2</sub>CO<sub>3</sub> content of KOH, type of Ti<sup>4+</sup> precursor, addition of an excess of Sr<sup>2+</sup> precursor.
- Identification of carbonate anion radical (*via in situ* EPR) as an active specie in the presence of SrTiO<sub>3</sub>-SrCO<sub>3</sub> catalyst under irradiation.
- Unravelling the stability issues of the SrCO<sub>3</sub>-containing catalyst in aqueous medium (dissolution of certain SrCO<sub>3</sub>) *via* Rietveld analysis (before and after reaction), and *via* assessing the inorganic carbon content of the reaction mixture before and after reaction.

In **Section 2.3**, there is provided an insight into the tuning of the selectivity of the SrTiO<sub>3</sub>-based photocatalyst during CO<sub>2</sub> reduction *by* modifying it *via* impregnation (NiO) or/and Au photo-deposition. Two support catalysts were used, namely commercial SrTiO<sub>3</sub> (IoliTec, notation: STO), and hydrothermally synthesized SrTiO<sub>3</sub>-SrCO<sub>3</sub> (~18 wt% SrCO<sub>3</sub>, notation: STO-SCO (HT)). Additional reference catalysts were analysed and further modified for comparison, such as commercial SrCO<sub>3</sub> (Merck, notation: SCO), SrTiO<sub>3</sub>-SrCO<sub>3</sub> prepared *via* suspension method using the previously mentioned commercial catalysts (~18 wt% SrCO<sub>3</sub>, notation: STO-SCO (SM)). While mainly CH<sub>4</sub> formation was observed over STO-SCO (HT) and NiO/STO-SCO (HT) catalysts, H<sub>2</sub> was generated over Au-STO-SCO (HT), and C<sub>2</sub>H<sub>6</sub> was produced over Au-NiO/STO-SCO (HT). Mainly CH<sub>4</sub> formation was observed in all the STO-based samples (i.e., STO, NiO/STO, Au-STO, Au-NiO/STO). To understand the reason behind the higher activity in the case of SrCO<sub>3</sub>-containing samples, the already reported charge transfer mechanisms were analysed and revised. The widely used and accepted mechanism in case of SrTiO<sub>3</sub>-SrCO<sub>3</sub> heterojunction assumes the translocation of electrons from the conduction band of SrTiO<sub>3</sub> to the conduction band of SrCO<sub>3</sub>. Therefore, CO<sub>2</sub> reduction hypothetically would take place over SrCO<sub>3</sub>, which is relatively unlikely. At the same time, it is essential to highlight that this approach does not consider neither the alignment of the Fermi level nor the formation of internal electric field at the contact between the two components. Hence, our formulated research question was related to the possibility of an alternative charge transfer mechanism in case of SrTiO<sub>3</sub>-SrCO<sub>3</sub>, where the Fermi level alignment and the establishment of built-in electric field would take place. Therefore, the work function (and implicitly the Fermi level) of the pure (SrTiO<sub>3</sub> and SrCO<sub>3</sub>) and doped (C-doped SrTiO<sub>3</sub> and Ti-doped SrCO<sub>3</sub>) materials was calculated. The computational results supported the hypothesis regarding to the Fermi level shift after the interaction between SrTiO<sub>3</sub> and SrCO<sub>3</sub>. This study also highlighted that the surface termination of SrTiO<sub>3</sub> (i.e., SrO- or TiO<sub>2</sub>-terminations) had a huge impact on its Fermi level (*via* DFT calculations), and in consequence on the mechanism during CO<sub>2</sub> reduction. It is assumed that the further differences in product formation, such as in case of Au-STO (product: CH<sub>4</sub>) *vs.* Au-STO-SCO (HT) (product: H<sub>2</sub>) might be given by the differences in the Fermi level of SrTiO<sub>3</sub> *vs.* SrTiO<sub>3</sub>-SrCO<sub>3</sub>. To sum it up, the following functionalities/roles were associated with the studied components: (i) SrCO<sub>3</sub> has a positive influence on the photocatalytic influence of SrTiO<sub>3</sub>, (ii) due to the low amount of NiO (~0.3 wt. %), its influence on either supports

(SrTiO<sub>3</sub>, SrTiO<sub>3</sub>-SrCO<sub>3</sub>) is not considerable, (iii) differences in the product formation in the case of Au-containing catalysts may be given by the different Fermi level alignment between Au and SrTiO<sub>3</sub>, Au and SrTiO<sub>3</sub>-SrCO<sub>3</sub>, respectively, (iv) the dimerization of C1 product is favourable in case of the simultaneous presence of Au and NiO over SrTiO<sub>3</sub>-SrCO<sub>3</sub>.

#### **Personal contributions:**

- Preparation and the assessment of photocatalytic CO<sub>2</sub> reduction activity for the following catalysts NiO/SrTiO<sub>3</sub>-SrCO<sub>3</sub>, Au-SrTiO<sub>3</sub>-SrCO<sub>3</sub>, Au-NiO/SrTiO<sub>3</sub>-SrCO<sub>3</sub>
- Identification of the factors which influences the photocatalytic CO<sub>2</sub> reduction pathway in the case of the studied samples, such as termination of SrTiO<sub>3</sub> in contact with SrCO<sub>3</sub>
- Suggestion of possible charge transfer mechanism in case of NiO/ SrTiO<sub>3</sub>-SrCO<sub>3</sub>, Au-SrTiO<sub>3</sub>-SrCO<sub>3</sub>, Au-NiO/SrTiO<sub>3</sub>-SrCO<sub>3</sub>.
- Establishment of structure-function correlations

In **Section 2.4.** the assessment of flow situation in a falling film microreactor prototype with open microchannels *via* experimental and numerical methods is presented. Self-developed method was implemented for the assessment of the flow distribution and residence time – *via* pulse input tracer experiment – using ethanol or water as solvent, and fluorescein as fluorescent tracer. Given by the poor wettability of the stainless steel microchannels when water was used at the inlet (as liquid phase), the split & curve structure and the microchannels were coated either with a thin titania (P25) or SrTiO<sub>3</sub> layer to assure improved hydrophilicity of the channels. Relatively uniform distribution of the liquid film was observed in both coated (in case of both water or ethanol) and uncoated (only in case of ethanol) microchannels. The experimentally estimated residence time values were higher than the empirically calculated ones. This already indicated the possibility of formation of a thicker liquid film in the microchannels than expected from the (empirical) calculations. Furthermore, 2D and 3D simulations were performed in ANSYS Fluent 2023R2 considering a representative portion of the microchannel using the Volume of Fluid multiphase model. The 3D simulation results confirmed the formation of thicker liquid film. An increase of liquid film thickness along the channel length was also observed. The increasing liquid film thickness along the channel length was correlated with the backflow phenomena and with the capillary effects in the microchannel. Based on the further 3D simulations, the following conclusions were drawn: (i) the plate inclination angle has a considerable influence on the stability of the liquid film thickness, (ii) the transversal wetted area is governed by the GLS contact angle at the sidewalls.

#### **Personal contributions:**

- Implementation of the slurry washcoating method (i.e., slurry composition and temperature applied during the thermal treatment) for coating of the microchannels with two catalysts, namely TiO<sub>2</sub>-P25 and SrTiO<sub>3</sub>.
- Implementation of a strategy for controlling the thickness of the catalyst layer *via* the mass of the applied (sprayed) catalyst slurry.

- Implementation of a self-developed pulse input tracer experiment for estimation of the residence time in the single channels (58 visible microchannels).
- Implementation of a self-developed method for the assessment of capillary forces.
- Implementation of strategies regarding to the estimation (calculation) of the liquid film thickness based on the holdup experiment, and pulse input tracer experiment.
- Implementation of the 2D and 3D multiphase simulations of the G-L phase in ANSYS Fluent considering a representative portion of one microchannel.
- The inclination angle of the reaction plate determines the flow stability (e.g., when the inclination angle ( $\theta$ ) was  $15^\circ$  - overflow, when  $\theta = 75^\circ$  - instable flow).
- Identification of parameters (in addition to the already known parameters) which have influence on the flow behaviour: GLS contact angle (which can be adjusted by the properties of the coating).
- Identification of backflow phenomena in microchannels based on experimental and numerical investigations.
- Establishment of correlations: increasing film thickness along the channel length – backflow phenomena – capillary effect.

**Section 2.5** presented a strategic kinetic analysis of the degradation of ciprofloxacin in aqueous solution in a falling film microreactor prototype with  $\text{TiO}_2$  (P25) or  $\text{SrTiO}_3$ -coated microchannels. Due to the unsatisfactory recyclability of the  $\text{SrTiO}_3$  catalysts during the consecutive flow experiments (i.e., deactivation), only the reference catalyst ( $\text{TiO}_2$  - P25) was further used for kinetic studies. The operating regime of the photoreactor was assessed through nondimensional numbers (Péclet, Damköhler II). The investigations highlighted, that heterogeneous concentration distribution was characteristic along the liquid film thickness. Therefore, the coupled mass and momentum conservation law was solved numerically for 2D case in MATLAB 2023a. The 2D model did not provide accurate prediction of the outlet concentration in the microchannels, therefore 3D model was implemented in ANSYS Fluent. Our investigations highlighted the importance of 3D model given by the sidewall effects in microchannels. The implemented 2D model can be used for the modeling of falling film reactors where the influence of sidewalls is negligible on the flow and on the mass transfer. The implemented 3D model can be applied for the modeling of falling film microreactors where heterogeneous concentration distribution is characteristic along the liquid film thickness.

#### **Personal contributions:**

- Assessment of external and internal mass transfer limitations *via* experimental and empirical methods.
- Description of the kinetics of ciprofloxacin degradation over  $\text{TiO}_2$ -P25 catalyst *via* the Langmuir-Hinshelwood (LH) model
- Implementation of 2-dimensional mathematical model of the liquid film in the microchannel considering both momentum and mass conservation laws.
- Discretization of the partial differential equation (for the 2D case) with the method of lines.

- Fitting of the LH adsorption constant ( $K_{LH}$ ) and LH kinetic rate constant ( $k_{LH}$ ) based on the implemented 2D model.
- Implementation of a simplified 3D model of the reactor in ANSYS Fluent.
- Determination of realistic and accurate kinetic parameters *via* fitting based on the 3D model in OptiSLang.

To sum it up, this PhD thesis may provide an insight on the favorable aspects related to the combination of experimental and computational investigations not only for flow studies, but also for the development of catalysts. I strongly believe that the ideas regarding to the presented self-implemented methods and the applied interdisciplinarity might be a guide for further developments.

## Chapter 4. Bibliography

- [1] N. László, B. Fisher, K. Hernadi, N. Krisztina, J. Vincze Photosynthetic Reaction Centres—from Basic Research to Application, *Notulae Scientia Biologicae*, 2 (2010) 07-13.
- [2] J. Lv, J. Xie, A.G.A. Mohamed, X. Zhang, Y. Feng, L. Jiao, E. Zhou, D. Yuan, Y. Wang, Solar utilization beyond photosynthesis, *Nature Reviews Chemistry*, 7 (2023) 91-105.
- [3] T. Szabó, M. Magyar, K. Hajdu, M. Dorogi, E. Nyerki, T. Tóth, M. Lingvay, G. Garab, K. Hernádi, L. Nagy, Structural and functional hierarchy in photosynthetic energy conversion—from molecules to nanostructures, *Nanoscale Research Letters*, 10 (2015) 1-12.
- [4] NASA, NASA Global Climate Change, 2024. Available from: <https://science.nasa.gov/climate-change/>. Last accessed on 05.02.2024, 10:15 CET
- [5] D. Raimi, Y. Zhu, R.G. Newell, B.C. Prest, A. Bergman, *Global Energy Outlook 2023: Sowing the Seeds of an Energy Transition*, 2023, 3-4.
- [6] P. Valbonesi, M. Profita, I. Vasumini, E. Fabbri, Contaminants of emerging concern in drinking water: Quality assessment by combining chemical and biological analysis, *Science of the Total Environment*, 758 (2021) 143624.
- [7] S. Daouk, N. Chèvre, N. Vernaz, C. Widmer, Y. Daali, S. Fleury-Souverain, Dynamics of active pharmaceutical ingredients loads in a Swiss university hospital wastewaters and prediction of the related environmental risk for the aquatic ecosystems, *Science of The Total Environment*, 547 (2016) 244-253.
- [8] Y. Aguas, M. Hincapie, P. Fernández-Ibáñez, M.I. Polo-López, Solar photocatalytic disinfection of agricultural pathogenic fungi (*Curvularia* sp.) in real urban wastewater, *Science of the total environment*, 607 (2017) 1213-1224.
- [9] R. Portela, R.F. Tessinari, S. Suarez, S.B. Rasmussen, M.D. Hernández-Alonso, M.C. Canela, P. Avila, B. Sánchez, Photocatalysis for continuous air purification in wastewater treatment plants: from lab to reality, *Environmental Science & Technology*, 46 (2012) 5040-5048.
- [10] J.O. de Brito Lira, H.G. Riella, N. Padoin, C. Soares, An overview of photoreactors and computational modeling for the intensification of photocatalytic processes in the gas-phase: state-of-art, *Journal of Environmental Chemical Engineering*, 9 (2021) 105068.
- [11] M. Tasbihi, M. Schwarze, R. Schomäcker, *Photocatalytic CO<sub>2</sub> Reduction and Beyond, Heterogeneous Photocatalysis: From Fundamentals to Applications in Energy Conversion and Depollution*, (Ed. J. Strunk), (2021) Wiley-VCH, Weinheim, Germany , 287-302.
- [12] Z. Sun, N. Talreja, H. Tao, J. Texter, M. Muhler, J. Strunk, J. Chen, Catalysis of carbon dioxide photoreduction on nanosheets: fundamentals and challenges, *Angewandte Chemie International Edition*, 57 (2018) 7610-7627.
- [13] R. Li, C. Li, *Photocatalytic water splitting on semiconductor-based photocatalysts*, *Advances in Catalysis* (Ed. C. Song), (2017) Academic Press, Amsterdam, Netherlands, 1-57.
- [14] J.Z. Bloh, R. Marschall, *Heterogeneous photoredox catalysis: reactions, materials, and reaction engineering*, *European Journal of Organic Chemistry*, 2017 (2017) 2085-2094.
- [15] D. Wang, M.A. Mueses, J.A.C. Márquez, F. Machuca-Martínez, I. Grčić, R.P.M. Moreira, G.L. Puma, Engineering and modeling perspectives on photocatalytic reactors for water treatment, *Water Research*, 202 (2021) 117421.

- [16] H. Eskandarloo, A. Badiei, Fabrication of an inexpensive and high efficiency microphotoreactor using CO<sub>2</sub> laser technique for photocatalytic water treatment applications, *Environmental technology*, 36 (2015) 1063-1073.
- [17] E. Colombo, M. Ashokkumar, Comparison of the photocatalytic efficiencies of continuous stirred tank reactor (CSTR) and batch systems using a dispersed micron sized photocatalyst, *RSC Advances*, 7 (2017) 48222-48229.
- [18] R. Binjhade, R. Mondal, S. Mondal, Continuous photocatalytic reactor: Critical review on the design and performance, *Journal of Environmental Chemical Engineering*, 10 (2022) 107746.
- [19] Z. Kusanov, B. Bakbolat, A. Baimenov, A. Issadykov, M. Yeleuov, C. Daulbayev, Photocatalysts for a sustainable future: Innovations in large-scale environmental and energy applications, *Science of The Total Environment*, 885 (2023) 163914.
- [20] F. Machuca Martinez, J.A. Colina Marquez, Photocatalysis process applied in order to eliminate recalcitrant compounds from industrial wastewater, (2012). patent publication, last accessed on 01.05.2024, <http://www.wipo.int/patentscope/search/en/WO2011055234>
- [21] S. Malato, J. Blanco, A. Vidal, C. Richter, Photocatalysis with solar energy at a pilot-plant scale: an overview, *Applied Catalysis B: Environmental*, 37 (2002) 1-15.
- [22] K. Shukla, S. Agarwalla, S. Duraiswamy, R.K. Gupta, Recent advances in heterogeneous micro-photoreactors for wastewater treatment application, *Chemical Engineering Science*, 235 (2021) 116511.
- [23] P. Watts, C. Wiles, Recent advances in synthetic micro reaction technology, *Chemical Communications*, (2007) 443-467.
- [24] N. Wang, X. Zhang, Y. Wang, W. Yu, H.L. Chan, Microfluidic reactors for photocatalytic water purification, *Lab on a Chip*, 14 (2014) 1074-1082.
- [25] H. Lindstrom, R. Wootton, A. Iles, High surface area titania photocatalytic microfluidic reactors, *AIChE journal*, 53 (2007) 695-702.
- [26] S. Das, V.C. Srivastava, Microfluidic-based photocatalytic microreactor for environmental application: a review of fabrication substrates and techniques, and operating parameters, *Photochemical & Photobiological Sciences*, 15 (2016) 714-730.
- [27] S.R. Pradhan, V. Nair, D.A. Giannakoudakis, D. Lisovytskiy, J.C. Colmenares, Design and development of TiO<sub>2</sub> coated microflow reactor for photocatalytic partial oxidation of benzyl alcohol, *Molecular Catalysis*, 486 (2020) 110884.
- [28] G. Dong, B. Chen, B. Liu, L.J. Hounjet, Y. Cao, S.R. Stoyanov, M. Yang, B. Zhang, Advanced oxidation processes in microreactors for water and wastewater treatment: Development, challenges, and opportunities, *Water Research*, 211 (2022) 118047.
- [29] D. Heggo, S. Ookawara, Multiphase photocatalytic microreactors, *Chemical Engineering Science*, 169 (2017) 67-77.
- [30] T.H. Rehm, S. Gros, P. Löb, A. Renken, Photonic contacting of gas-liquid phases in a falling film microreactor for continuous-flow photochemical catalysis with visible light, *Reaction Chemistry & Engineering*, 1 (2016) 636-648.
- [31] N. Steinfeldt, N. Kockmann, Experimental and Numerical Characterization of Transport Phenomena in a Falling Film Microreactor with Gas-Liquid Reaction, *Industrial & Engineering Chemistry Research*, 59 (2020) 4033-4047.

- [32] V. Hessel, P. Angeli, A. Gavriilidis, H. Löwe, Gas– liquid and gas– liquid– solid microstructured reactors: contacting principles and applications, *Industrial & Engineering Chemistry Research*, 44 (2005) 9750-9769.
- [33] V. Hessel, P. Löb, K. Mevissen, F. Schönfeld, Pseudo 3-D simulation of a falling film microreactor based on realistic channel and film profiles, *Chemical Engineering Science*, 63 (2008) 5149-5159.
- [34] B. Stephan, L. Ludovic, W. Dominique, Modelling of a falling thin film deposited photocatalytic step reactor for water purification: Pesticide treatment, *Chemical Engineering Journal*, 169 (2011) 216-225.
- [35] G. Li Puma, P.L. Yue, Enhanced photocatalysis in a pilot laminar falling film slurry reactor, *Industrial & Engineering Chemistry Research*, 38 (1999) 3246-3254.
- [36] Y. Boyjoo, M. Ang, V. Pareek, Some aspects of photocatalytic reactor modeling using computational fluid dynamics, *Chemical Engineering Science*, 101 (2013) 764-784.
- [37] R.R. Solís, J. Bedia, J.J. Rodríguez, C. Belver, A review on alkaline earth metal titanates for applications in photocatalytic water purification, *Chemical Engineering Journal*, 409 (2021) 128110.
- [38] L. Bai, Q. Xu, Z. Cai, Synthesis of Ag@ AgBr/CaTiO<sub>3</sub> composite photocatalyst with enhanced visible light photocatalytic activity, *Journal of Materials Science: Materials in Electronics*, 29 (2018) 17580-17590.
- [39] L.F. da Silva, O.F. Lopes, V.R. de Mendonça, K.T. Carvalho, E. Longo, C. Ribeiro, V.R. Mastelaro, An understanding of the photocatalytic properties and pollutant degradation mechanism of SrTiO<sub>3</sub> nanoparticles, *Photochemistry and Photobiology*, 92 (2016) 371-378.
- [40] S. Kappadan, T.W. Gebreab, S. Thomas, N. Kalarikkal, Tetragonal BaTiO<sub>3</sub> nanoparticles: An efficient photocatalyst for the degradation of organic pollutants, *Materials Science in Semiconductor Processing*, 51 (2016) 42-47.
- [41] R. Wang, S. Ni, G. Liu, X. Xu, Hollow CaTiO<sub>3</sub> cubes modified by La/Cr co-doping for efficient photocatalytic hydrogen production, *Applied catalysis B: environmental*, 225 (2018) 139-147.
- [42] K. Yu, C. Zhang, Y. Chang, Y. Feng, Z. Yang, T. Yang, L.-L. Lou, S. Liu, Novel three-dimensionally ordered macroporous SrTiO<sub>3</sub> photocatalysts with remarkably enhanced hydrogen production performance, *Applied Catalysis B: Environmental*, 200 (2017) 514-520.
- [43] T. Chen, J. Meng, S. Wu, J. Pei, Q. Lin, X. Wei, J. Li, Z. Zhang, Room temperature synthesized BaTiO<sub>3</sub> for photocatalytic hydrogen evolution, *Journal of Alloys and Compounds*, 754 (2018) 184-189.
- [44] G. Xing, L. Zhao, T. Sun, Y. Su, X. Wang, Hydrothermal derived nitrogen doped SrTiO<sub>3</sub> for efficient visible light driven photocatalytic reduction of chromium (VI), *SpringerPlus*, 5 (2016) 1-13.
- [45] T. Soltani, X. Zhu, A. Yamamoto, S.P. Singh, E. Fudo, A. Tanaka, H. Kominami, H. Yoshida, Effect of transition metal oxide cocatalyst on the photocatalytic activity of Ag loaded CaTiO<sub>3</sub> for CO<sub>2</sub> reduction with water and water splitting, *Applied Catalysis B: Environmental*, 286 (2021) 119899.
- [46] C. Luo, J. Zhao, Y. Li, W. Zhao, Y. Zeng, C. Wang, Photocatalytic CO<sub>2</sub> reduction over SrTiO<sub>3</sub>: Correlation between surface structure and activity, *Applied Surface Science*, 447 (2018) 627-635.

- [47] X. Peng, G. Yang, Y. Shi, Y. Zhou, M. Zhang, S. Li, Box–Behnken design based statistical modeling for the extraction and physicochemical properties of pectin from sunflower heads and the comparison with commercial low-methoxyl pectin, *Scientific Reports*, 10 (2020) 3595.
- [48] E.-Z. Kedves, I. Székely, L. Baia, M. Baia, A. Csavdári, Z. Pap, The comparison of the photocatalytic performance shown by  $\text{TiO}_2$  and  $\text{TiO}_2/\text{WO}_3$  composites—a parametric and kinetic study, *Journal of Nanoscience and Nanotechnology*, 19 (2019) 356-365.
- [49] A. Mehrizad, P. Gharbani, Novel ZnS/carbon nanofiber photocatalyst for degradation of rhodamine 6G: kinetics tracking of operational parameters and development of a kinetics model, *Photochemistry and Photobiology*, 93 (2017) 1178-1186.
- [50] G. Palmisano, V. Loddo, V. Augugliaro, M. Bellardita, G.C. Roda, F. Parrino, Validation of a two-dimensional modeling of an externally irradiated slurry photoreactor, *Chemical Engineering Journal*, 262 (2015) 490-498.
- [51] W. Dong, G. Zhao, B. Song, G. Xu, J. Zhou, G. Han, Surfactant-free fabrication of  $\text{CaTiO}_3$  butterfly-like dendrite via a simple one-step hydrothermal route, *CrystEngComm*, 14 (2012) 6990-6997.
- [52] M. Hernández-Alonso, S. García-Rodríguez, B. Sánchez, J. Coronado, Revisiting the hydrothermal synthesis of titanate nanotubes: new insights on the key factors affecting the morphology, *Nanoscale*, 3 (2011) 2233-2240.
- [53] S. Ebnesajjad, P.R. Khaladkar, *Fluoropolymer applications in the chemical processing industries: the definitive user's guide and handbook* (2017). William Andrew, Oxford, United Kingdom, 10-15.
- [54] W. Cen, T. Xiong, C. Tang, S. Yuan, F. Dong, Effects of morphology and crystallinity on the photocatalytic activity of  $(\text{BiO})_2\text{CO}_3$  nano/microstructures, *Industrial & Engineering Chemistry Research*, 53 (2014) 15002-15011.
- [55] C. Han, J. Liu, W. Yang, Q. Wu, H. Yang, X. Xue, Photocatalytic activity of  $\text{CaTiO}_3$  synthesized by solid state, sol–gel and hydrothermal methods, *Journal of Sol-Gel Science and Technology*, 81 (2017) 806-813.
- [56] J. Zhang, K. Huang, L. Yuan, S. Feng, Mineralizer effect on facet-controllable hydrothermal crystallization of perovskite structure  $\text{YbFeO}_3$  crystals, *CrystEngComm*, 20 (2018) 470-476.
- [57] A. Ward, L. Tordai, Time-dependence of boundary tensions of solutions I. The role of diffusion in time-effects, *The Journal of Chemical Physics*, 14 (1946) 453-461.
- [58] M. Nasr, C. Eid, R. Habchi, P. Miele, M. Bechelany, Recent progress on titanium dioxide nanomaterials for photocatalytic applications, *ChemSusChem*, 11 (2018) 3023-3047.
- [59] J.-I. Fujisawa, T. Eda, M. Hanaya, Comparative study of conduction-band and valence-band edges of  $\text{TiO}_2$ ,  $\text{SrTiO}_3$ , and  $\text{BaTiO}_3$  by ionization potential measurements, *Chemical Physics Letters*, 685 (2017) 23-26.
- [60] G. Wu, P. Li, D. Xu, B. Luo, Y. Hong, W. Shi, C. Liu, Hydrothermal synthesis and visible-light-driven photocatalytic degradation for tetracycline of Mn-doped  $\text{SrTiO}_3$  nanocubes, *Applied Surface Science*, 333 (2015) 39-47.
- [61] H.L. Chou, B.J. Hwang, C.L. Sun, *Catalysis in fuel cells and hydrogen production, New and Future Developments in Catalysis: Batteries, Hydrogen Storage and Fuel Cells*, Elsevier BV2013, 217-270.

- [62] A. Kudo, Y. Miseki, Heterogeneous photocatalyst materials for water splitting, *Chemical Society Reviews*, 38 (2009) 253-278.
- [63] G. Canu, V. Buscaglia, Hydrothermal synthesis of strontium titanate: thermodynamic considerations, morphology control and crystallisation mechanisms, *CrystEngComm*, 19 (2017) 3867-3891.
- [64] R. Marschall, A. Mukherji, A. Tanksale, C. Sun, S.C. Smith, L. Wang, G.Q.M. Lu, Preparation of new sulfur-doped and sulfur/nitrogen co-doped CsTaWO<sub>6</sub> photocatalysts for hydrogen production from water under visible light, *Journal of Materials Chemistry*, 21 (2011) 8871-8879.
- [65] B. Mei, A. Pougin, J. Strunk, Influence of photodeposited gold nanoparticles on the photocatalytic activity of titanate species in the reduction of CO<sub>2</sub> to hydrocarbons, *Journal of Catalysis*, 306 (2013) 184-189.
- [66] D. Jiang, X. Sun, X. Wu, L. Shi, F. Du, Hydrothermal synthesis of single-crystal Cr-doped SrTiO<sub>3</sub> for efficient visible-light responsive photocatalytic hydrogen evolution, *Materials Research Express*, 7 (2020) 015047.
- [67] A. Márquez-Herrera, V.M. Ovando-Medina, B.E. Castillo-Reyes, M. Meléndez-Lira, M. Zapata-Torres, N. Saldaña, A novel synthesis of SrCO<sub>3</sub>-SrTiO<sub>3</sub> nanocomposites with high photocatalytic activity, *Journal of nanoparticle research*, 16 (2014) 1-10.
- [68] N. Zhang, J. Li, G. Liu, X. Chen, K. Jiang, Photodegradation of diclofenac in aqueous solution by simulated sunlight irradiation: kinetics, thermodynamics and pathways, *Water Science and Technology*, 75 (2017) 2163-2170.
- [69] S. Jin, G. Dong, J. Luo, F. Ma, C. Wang, Improved photocatalytic NO removal activity of SrTiO<sub>3</sub> by using SrCO<sub>3</sub> as a new co-catalyst, *Applied Catalysis B: Environmental*, 227 (2018) 24-34.
- [70] F.A. Villamena, *EPR Spin Trapping in Reactive Species Detection in Biology* (2017). Elsevier. Amsterdam, The Netherlands, 163-202.
- [71] Z. Li, P. Zheng, W. Zhang, S. Gong, L. Zhu, J. Xu, F. Rao, X. Xie, G. Zhu, Constructing SrCO<sub>3</sub>/SrTiO<sub>3</sub> nanocomposites with highly selective photocatalytic CO<sub>2</sub>-to-CO reduction, *Colloids and Surfaces A: Physicochemical and Engineering Aspects*, 650 (2022) 129686.
- [72] X. Pan, X. Chen, Z. Yi, Photocatalytic oxidation of methane over SrCO<sub>3</sub> decorated SrTiO<sub>3</sub> nanocatalysts via a synergistic effect, *Physical Chemistry Chemical Physics*, 18 (2016) 31400-31409.
- [73] B. Boga, N. Steinfeldt, N.G. Moustakas, T. Peppel, H. Lund, J. Rabeah, Z. Pap, V.-M. Cristea, J. Strunk, Role of SrCO<sub>3</sub> on photocatalytic performance of SrTiO<sub>3</sub>-SrCO<sub>3</sub> composites, *Catalysts*, 12 (2022) 978.
- [74] A. Pougin, M. Dilla, J. Strunk, Identification and exclusion of intermediates of photocatalytic CO<sub>2</sub> reduction on TiO<sub>2</sub> under conditions of highest purity, *Physical Chemistry Chemical Physics*, 18 (2016) 10809-10817.
- [75] C. Xin, M. Hu, K. Wang, X. Wang, Significant enhancement of photocatalytic reduction of CO<sub>2</sub> with H<sub>2</sub>O over ZnO by the formation of basic zinc carbonate, *Langmuir*, 33 (2017) 6667-6676.
- [76] J.F. Fernando, M.P. Shortell, C.J. Noble, J.R. Harmer, E.A. Jaatinen, E.R. Waclawik, Controlling Au photodeposition on large ZnO nanoparticles, *ACS Applied Materials & Interfaces*, 8 (2016) 14271-14283.

- [77] N.G. Moustakas, M. Klahn, B.T. Mei, A. Pougin, M. Dilla, T. Peppel, S. Ristig, J. Strunk, A high-purity gas–solid photoreactor for reliable and reproducible photocatalytic CO<sub>2</sub> reduction measurements, *HardwareX*, 15 (2023) e00448.
- [78] T. Sreethawong, Y. Suzuki, S. Yoshikawa, Photocatalytic evolution of hydrogen over mesoporous TiO<sub>2</sub> supported NiO photocatalyst prepared by single-step sol–gel process with surfactant template, *International Journal of Hydrogen Energy*, 30 (2005) 1053-1062.
- [79] R. Vinoth, P. Karthik, K. Devan, B. Neppolian, M. Ashokkumar, TiO<sub>2</sub>–NiO p–n nanocomposite with enhanced sonophotocatalytic activity under diffused sunlight, *Ultrasonics Sonochemistry*, 35 (2017) 655-663.
- [80] S. Cai, J. Chen, Q. Li, H. Jia, Enhanced photocatalytic CO<sub>2</sub> reduction with photothermal effect by cooperative effect of oxygen vacancy and Au cocatalyst, *ACS Applied Materials & Interfaces*, 13 (2021) 14221-14229.
- [81] A.I. Rabee, D. Zhao, S. Cisneros, C.R. Kreyenschulte, V. Kondratenko, S. Bartling, C. Kubis, E.V. Kondratenko, A. Brückner, J. Rabeah, Role of interfacial oxygen vacancies in low-loaded Au-based catalysts for the low-temperature reverse water gas shift reaction, *Applied Catalysis B: Environmental*, 321 (2023) 122083.
- [82] H. Sun, J. He, J. Wang, S.-Y. Zhang, C. Liu, T. Sritharan, S. Mhaisalkar, M.-Y. Han, D. Wang, H. Chen, Investigating the multiple roles of polyvinylpyrrolidone for a general methodology of oxide encapsulation, *Journal of the American Chemical Society*, 135 (2013) 9099-9110.
- [83] Y. Chen, J. Kang, B. Chen, B. Gao, L. Liu, X. Liu, Y. Wang, L. Wu, H. Yu, J. Wang, Microscopic mechanism for unipolar resistive switching behaviour of nickel oxides, *Journal of Physics D: Applied Physics*, 45 (2012) 065303.
- [84] S. Linic, P. Christopher, D.B. Ingram, Plasmonic-metal nanostructures for efficient conversion of solar to chemical energy, *Nature Materials*, 10 (2011) 911-921.
- [85] J.B. Priebe, M. Karnahl, H. Junge, M. Beller, D. Hollmann, A. Brückner, Water reduction with visible light: synergy between optical transitions and electron transfer in Au-TiO<sub>2</sub> catalysts visualized by in situ EPR spectroscopy, *Angewandte Chemie International Edition*, 52 (2013).
- [86] P. Naliwajko, T. Peppel, J. Strunk, Thermal and light induced infrared blackening of ZnO revisited: Rediscovery of fundamental scientific knowledge, *Reaction Kinetics, Mechanisms and Catalysis*, 135 (2022) 2291-2305.
- [87] X. Chang, T. Wang, J. Gong, CO<sub>2</sub> photo-reduction: insights into CO<sub>2</sub> activation and reaction on surfaces of photocatalysts, *Energy & Environmental Science*, 9 (2016) 2177-2196.
- [88] S. Han, X. Li, Y. Tan, Y. Huang, Z. Wu, M. Wang, W. Ho, S.-c. Lee, In-situ self-sacrificed fabrication of insulator-based SrTiO<sub>3</sub>/SrCO<sub>3</sub> heterojunction interface for gaseous HCHO and NO photocatalytic degradation, *Applied Surface Science*, 612 (2023) 155806.
- [89] K. Domen, A. Kudo, T. Onishi, N. Kosugi, H. Kuroda, Photocatalytic decomposition of water into hydrogen and oxygen over nickel (II) oxide-strontium titanate (SrTiO<sub>3</sub>) powder. 1. Structure of the catalysts, *The Journal of Physical Chemistry*, 90 (1986) 292-295.
- [90] W. Guo, J. Huang, W.D. Wei, Plasmonic metal/semiconductor heterostructures, *Plasmonic Catalysis: From Fundamentals to Applications*, (Eds. H.C.P. Camargo, & E. Cortés) (2021), Wiley-VCH, Weinheim, Germany, 295-322

- [91] L. Liao, G. Xie, X. Xie, N. Zhang, Advances in modulating the activity and selectivity of photocatalytic CO<sub>2</sub> reduction to multicarbon products, *The Journal of Physical Chemistry C*, 127 (2023) 2766-2781.
- [92] B.K. Vankayala, P. Löb, V. Hessel, G. Menges, C. Hofmann, D. Metzke, U. Krttschil, H.-J. Kost, Scale-up of process intensifying falling film microreactors to pilot production scale, *International Journal of Chemical Reactor Engineering*, 5 (2007).
- [93] W. Ehrfeld, V. Hessel, H. Löwe, *Microreactors: New Technology for Modern Chemistry 2000*, Wiley, Weinheim, Germany, 244-247.
- [94] D.F. Fletcher, B.S. Haynes, J. Aubin, C. Xuereb, Modeling of microfluidic devices, *Micro process engineering, A comprehensive handbook, Vol 1*, (V. Hessel, A. Renken, J.C. Schouten, J.-I. Yoshida, Eds.) (2009) Wiley-VCH, Weinheim, Germany, 117-144.
- [95] O. Shvydkiv, K. Jaehnisch, N. Steinfeldt, A. Yavorsky, M. Oelgemoeller, Visible-light photooxygenation of  $\alpha$ -terpinene in a falling film microreactor, *Catalysis Today*, 308 (2018) 102-118.
- [96] J.-M. Commenge, T. Obein, G. Genin, X. Framboisier, S. Rode, V. Schanen, P. Pitiot, M. Matlosz, Gas-phase residence time distribution in a falling-film microreactor, *Chemical Engineering Science*, 61 (2006) 597-604.
- [97] N. Kockmann, Microfluidic networks, *Micro Process Engineering*, (2009) 41-59.
- [98] R.B. Bird, Stewart, W.E., Lightfoot, E.N., *Transport phenomena, Second Edition*. (2002), John Wiley & Sons, USA, 42-46.
- [99] V. Hessel, S. Hardt, H. Löwe, A multi-faceted, hierarchic analysis of chemical micro process technology: In, *Chemical Micro Process Engineering*, (2004), Wiley-VCH, Weinheim, Germany, 66-124.
- [100] A.B. Vir, S.R. Kulkarni, J. Picardo, A. Sahu, S. Pushpavanam, Holdup characteristics of two-phase parallel microflows, *Microfluidics and Nanofluidics*, 16 (2014) 1057-1067.
- [101] A. Kögel, N. Aksel, Stability of the channel flow—New phenomena in an old problem, *Acta Mechanica*, 231 (2020) 1063-1082.
- [102] A.D. Anastasiou, A. Gavriilidis, A.A. Mouza, Study of the hydrodynamic characteristics of a free flowing liquid film in open inclined microchannels, *Chemical Engineering Science*, 101 (2013) 744-754.
- [103] M. Rietz, B. Scheid, R. Kneer, Dynamics of falling films under the influence of a destabilizing body force, *Lehrstuhl für Wärme-und Stoffübertragung*, 2020.
- [104] D.H. Sharp, An overview of Rayleigh-Taylor instability, *Physica D: Nonlinear Phenomena*, 12 (1984) 3-18.
- [105] R. Tröger, H. Ren, D. Yin, C. Postigo, P.D. Nguyen, C. Baduel, O. Golovko, F. Been, H. Joerss, M.R. Boleda, What's in the water?—Target and suspect screening of contaminants of emerging concern in raw water and drinking water from Europe and Asia, *Water Research*, 198 (2021) 117099.
- [106] T. Mathai, T. Pal, N. Prakash, S. Mukherji, Portable biosensor for the detection of enrofloxacin and ciprofloxacin antibiotic residues in food, body fluids, environmental and wastewater samples, *Biosensors and Bioelectronics*, 237 (2023) 115478.